



## Modeling diffusive phase transformation and fracture in viscoplastic materials

Ethel Djeumen<sup>a,b,\*</sup>, Gergely Molnár<sup>a</sup>, Nicolas Tardif<sup>a</sup>, Michel Coret<sup>c</sup>, Jean Desquines<sup>b</sup>, Tatiana Taurines<sup>b</sup>, Marie-Christine Baietto<sup>a</sup>

<sup>a</sup> Univ Lyon, INSA-Lyon, CNRS UMR5259, LaMCoS, 69621, France

<sup>b</sup> IRSN, PSN-RES, Cadarache, Saint Paul lez Durance, 13115, France

<sup>c</sup> Univ Nantes, Ecole Centrale de Nantes, CNRS UMR6183, GeM, 44000, Nantes, France

### ARTICLE INFO

#### Keywords:

Multiphase-field model  
Multiphysical couplings  
Viscoplasticity  
Diffusion  
Phase transformation  
Fracture

### ABSTRACT

In recent years, the phase-field method has attracted a lot of attention and has emerged as one of the most efficient tools for modeling fracture and phase transformation. The phase-field method is based on the regularization of discontinuities which allows the resolution of complex problems using classical numerical methods. A multiphase-field model which is essential for describing crack propagation in non-static heterogeneous materials is still missing. In this work, we fill this gap by combining the fracture phase-field approach based on Griffith's theory with the phase-field approach for diffusive phase transformation in viscoplastic materials. Several benchmark examples of increasing complexity demonstrate the effect of viscoplasticity and diffusive phase transformation on fracture behavior based on the critical loading, energy density until failure and crack topology. We show that viscoplastic activity at the crack tip mitigates the effect of pre-existing defects on mechanical strength. In a heterogeneous case, it is shown that viscoplastic activity introduces an intermediate fracture response between the reference behavior, which does not take into consideration the phase transformation-induced residual stresses, and the elastic behavior, which integrates these residual stresses by taking into account only the elasticity. The interaction between the heterogeneities and the crack topology is also highlighted.

### 1. Introduction

One of the most feared failure modes in engineering is fracture as it can occur suddenly and potentially lead to catastrophic consequences. The combined action of mechanical stresses and phase transformations can significantly affect the response of structures. For example, in case of a loss of coolant accident in a pressurized water nuclear reactor, an interaction between oxygen diffusion, oxidation, creep and cracking phenomena is observed (Desquines et al., 2021; Chosson et al., 2016; Thieurmél et al., 2019; Dominguez, 2018; Campello et al., 2017). Modeling of the mechanical behavior coupled with the phase transformation of a multilayer material is therefore an important issue. This work aims at developing a numerical platform coupling nonlinear mechanical behavior to phase transformation and fracture.

The phase-field approach is used to represent fracture and phase transformation. This approach based on energy minimization lends itself well to numerical implementation and seems to be the simplest tool for modeling multi-physics problems in a single framework (Wu et al., 2020). The phase-field approach is well suited for phase transformation

and easily allows the consideration of the diffusion of chemical species. Regarding fracture, the phase-field approach is suitable for brittle fracture. However, it is well known that ductile and brittle fracture involve different mechanisms. In this work, the fracture phase-field approach is chosen to represent both brittle and ductile fracture responses. The description of the material aspects related to the ductile fracture is not treated and it is assumed that the phases are homogeneous.

The phase-field approach is employed in order to deal with singularities such as fracture and phase transformation (Singer-Loginova and Singer, 2008; Ambati et al., 2015b). It has become increasingly popular in recent years due to its simplicity and flexibility. The main idea behind the phase-field approach is to smooth singularities in order to describe them with auxiliary scalar fields.

In the phase-field approach for phase transformation, the sharp interface is replaced by a diffuse interface of non-zero thickness ( $\delta$ ). With this regularization, the phases are described by a continuous order parameter ( $\phi$ ) governing the local interface kinetics. This phase-field approach has a decisive advantage compared to sharp interface

\* Corresponding author at: Univ Lyon, INSA-Lyon, CNRS UMR5259, LaMCoS, 69621, France.

E-mail addresses: [ethel-borel.djeumen-nkwechen@insa-lyon.fr](mailto:ethel-borel.djeumen-nkwechen@insa-lyon.fr) (E. Djeumen), [gergely.molnar@insa-lyon.fr](mailto:gergely.molnar@insa-lyon.fr) (G. Molnár).

## Nomenclature

$\mathcal{H}$	History field
$\delta$	Interface thickness (phase transition)
$\gamma$	Fracture surface density
$\lambda_i, \mu_i$	Lamé's elastic parameters
$\omega$	Interface energy
$\phi$	Order parameter
$\psi$	Helmholtz free energy density
$\psi_0^+$	Tensile component of the elastic strain energy density
$\psi_0^-$	Compression component of the elastic strain energy density
$\psi^{ch}$	Chemical free energy density
$\psi^{el}$	Stored elastic strain energy density
$\psi_c$	Fracture threshold energy
$\sigma$	Cauchy stress tensor
$\varepsilon$	Total strain tensor
$\varepsilon_i^*$	Eigenstrain tensor
$\varepsilon^{el}$	Elastic strain tensor
$\varepsilon_i^{vp}$	Viscoplastic strain tensor
$f_v$	Body force
$t$	Boundary force
$\mathbf{u}$	Displacement field
$A_i, n_i$	Norton's viscoplastic parameters
$c$	Concentration field
$d$	Damage variable
$g(d)$	Degradation function
$g_c$	Critical fracture surface energy
$k_i$	Curvature of the free energy density
$l_c$	Fracture length scale
$p$	Numerical stability number

models as explicit interface tracking is not required. Sharp interface models are not suitable when dealing with complex morphological evolutions because the interface tracking at each time step becomes computationally quite unfeasible.

The phase-field approach for phase transformation can be used to model both microstructures and mesoscale complex morphological evolutions such as grain-boundary evolution (Suwa et al., 2007; Moelans et al., 2008; Bhattacharya et al., 2020) and solidification (Labergère et al., 2021; Asle Zaeem et al., 2013). It can also be coupled with other physical ingredients such as elasticity (Düsing and Mahnken, 2019; Wang et al., 1993b; Dreyer and Müller, 2000), plasticity (Ammar et al., 2009a; Zhao et al., 2018) and viscoplasticity (de Rancourt et al., 2016; Cottura et al., 2012).

Similarly, in the fracture phase-field approach, the sharp crack is replaced by a regularized diffused damage. In order to mathematically tackle the problem, a length scale ( $l_c$ ) is introduced, which controls the magnitude of the damage penetration into a solid phase. A diffuse damage variable ( $d$ ) connects broken and unbroken regions. The fracture phase-field approach is based on the original description of Griffith for homogeneous brittle materials. Griffith (1924, 1921) suggested that a pre-existing crack can only propagate if the released potential energy per unit surface is greater than a critical value. The critical energy release rate is postulated to be a material constant that indicates its fracture toughness. The main advantage of the fracture phase-field approach is its simplicity. Compared to discrete methods such as the cohesive zone model (Zhou and Molinari, 2004; Falk et al., 2001), the so-called strong discontinuity technique (Huespe et al., 2006) or the extended finite element method (Elguedj et al., 2006; Moës et al.,

1999; Réthoré et al., 2005; Gravouil et al., 2011), the diffused damage models (such as the phase-field or the thick level set approach (Moës et al., 2011)) provide a suitable framework for solving the problem with classical numerical methods without requiring special criteria or numerical tools. Ambati et al. (2015b) gives a detailed overview of the existing brittle fracture phase-field models. The fracture phase-field provides a simulation framework to adequately describe crack initiation, propagation, curvilinear crack paths, branching or coalescence (Molnár and Gravouil, 2017). The effect of plasticity (Molnár et al., 2020a; Zhang et al., 2018; Duda et al., 2015; Ambati et al., 2015a), viscoplasticity (Shanthraj et al., 2016), hyperelasticity (Peng et al., 2020; Yin et al., 2019; Mandal et al., 2020), fatigue (Lo et al., 2019; Mesgarnejad et al., 2019), and chemical diffusion (Miehe et al., 2016b; Schneider et al., 2014; Nguyen et al., 2018) can also be included in a thermodynamically consistent manner.

The diffusive phase transformations that heterogeneous materials undergo can significantly affect their fracture behavior. However, a general approach to study the fracture behavior of these non-static heterogeneous materials is still missing. Schneider et al. (2016) proposed a multiphase-field model that combines the fracture phase-field and the phase-field for the phase transformation process, but the application of this model is limited to diffusionless transformation such as martensitic transformation as the diffusion process is not modeled.

In this work, we combine the fracture phase-field approach with the phase-field approach for diffusive phase transformation processes to study the fracture behavior of solid-state materials undergoing mesoscale diffusive phase transformations. Compared to previous works of Schneider et al. (2016), the proposed model is more generalized by including in the formulation the chemical diffusion which is the driving force of the diffusive phase transformation. Four physical phenomena are therefore considered including fracture, diffusion, phase transformation and viscoplasticity. The simultaneous consideration of these four physics is important for the study of the combined action of a mechanical stress and an aggressive environment encountered in several applications in industry. For example, the phenomenon of loss of coolant accident in a nuclear reactor (Campello et al., 2017; Desquines et al., 2021; Chosson et al., 2016; Dominguez, 2018; Thieumel et al., 2019) or the well-known phenomenon of stress corrosion cracking (Sieradzki and Newman, 1987). The formulation of the model is carried out in an appropriate framework that easily allows its extension with new physical ingredients or additional couplings.

The present paper is structured as follows. Section 2 presents the consistent framework combining the various physical phenomena being modeled (fracture, diffusion, phase transformation and viscoplasticity) into a single multiphase-field model. The theoretical background and modeled couplings are specified. In Section 3, through several benchmark examples of increasing complexity, the proposed model is used to investigate the effect of viscoplastic activity and diffuse phase transformation on the fracture behavior. The impact on fracture behavior is assessed by examining the critical loading, energy density until failure and crack topology. Finally, Section 4 concludes this work.

## 2. Methods

The phase-field approach for fracture and phase transformation are based on the diffuse representation of the discontinuity in the volume as illustrated in Fig. 1. For fracture, we define a diffuse damage variable  $d$  which connects broken ( $d = 1$ ) and unbroken ( $d = 0$ ) regions. An internal length scale ( $l_c$ ) controls the magnitude of the damage penetration. In the same way, an order parameter ( $\phi$ ) is used to describe the phase  $a$  ( $\phi = 1$ ) and phase  $b$  ( $\phi = 0$ ) regions of a binary material. A non-zero interface thickness ( $\delta$ ) controls the width of the smooth transition between both solid phases.

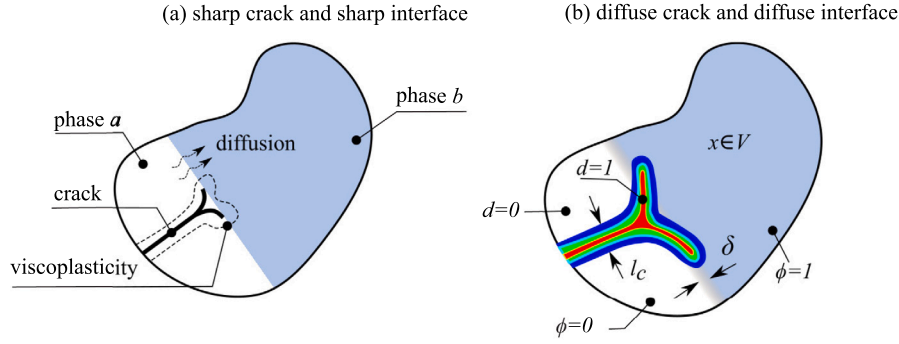


Fig. 1. (a) Schematic illustration of the idealized physical problem and its corresponding regularization (b).  $l_c$  and  $\delta$  respectively control the width of the damaged and the interface regions.

The model developed in this work makes it possible to simultaneously solve the displacement problem with viscoplastic activity, the mass transport or diffusion, the fracture and the phase transformation problems. In general, the total energy of the multi-physics problem composed of a mechanical ( $\mathcal{L}^u$ ), chemical ( $\mathcal{L}^{ch}$ ) and fracture ( $\mathcal{L}^d$ ) part can be written as :

$$\mathcal{L}(\nabla \mathbf{u}, \phi, c, d) = \mathcal{L}^u(\nabla \mathbf{u}, \phi, c, d) + \mathcal{L}^{ch}(\nabla \mathbf{u}, \phi, c, d) + \mathcal{L}^d(\nabla \mathbf{u}, \phi, c, d) \quad (1)$$

where  $\mathbf{u}$ ,  $\phi$ ,  $c$ ,  $d$  respectively the displacement vector, the order parameter, the concentration of the diffusing chemical species and the damage variable. Eq. (1) is written in the general case considering all possible interaction between the modeled physics. In the following, only the couplings summarized in Fig. 2 are considered. The damage reduces the stiffness of the material, while the elastic (undamaged) strain energy contributes to the crack surface opening. The phase transformation is driven by the free energy which is composed of the stored elastic strain energy and chemical energy. In the interface where the two phases coexist, a mixing or interpolation method is used to include the energy contributions of both phases. Several couplings are taken into account but the list is not exhaustive. However, the formulation is proposed in a framework that allows the introduction of new couplings in a relatively easy way. The effect of the diffusing species on the mechanical and fracture properties (Le Saux et al., 2018; Nguyen et al., 2017) and the coupling between diffusion and viscoplasticity (Le Claire and Rabinovitch, 1981, 1982, 1983) are not taken into account. We also neglect the explicit coupling between phase transformation and fracture, thus their constitutive laws can be formulated separately. Griffith's theory (Griffith, 1921) is employed for the fracture phase-field approach, while the Allen–Cahn theory (Allen and Cahn, 1979) is used for phase transformation phase-field.

In fracture phase-field, the mechanical energy is used to control crack surface opening. The consideration of the contribution of plastic or viscoplastic dissipated energy to fracture is controversial in the literature (Molnár et al., 2020a). Some authors do not include the effect of plastic (Ambati et al., 2015a) or viscoplastic (Shanthraj et al., 2016) energy on the crack surface opening while others do (Fang et al., 2019; Badnava et al., 2017). This is a question of scale. Usually, it is assumed that very small-scale plasticity can cause void formation, leading to macroscopic cracks, for example, when the characteristic size of the model approaches the grain size. In this work, only the stored elastic strain energy contributes to the crack surface opening while viscoplasticity remains an independent dissipation.

In phase transformation phase-field, the so-called free energy, which contains both stored elastic strain energy and chemical energy, is used to govern the phase transformation. The motivation for adding a mechanical effect in the phase transformation problem comes from the idea that a strain accommodation leads to a development of certain optimal microstructures (Khachatryan and Shatalov, 1969).

In the case of an unstable crack, the monolithic solution of the fully coupled displacement and fracture problem becomes unstable.

Therefore, the displacement problem is weakly coupled to the evolution of fracture topology using the staggered scheme proposed by Miehe et al. (2010a). As shown in Fig. 3, at each increment the displacement problem is solved on the basis of the last converged fracture topology and vice versa.

### 2.1. Displacement problem

The displacement problem is solved under the following assumptions:

- damage only reduces the tensile stiffness, the compressive stiffness is not affected,
- the newly formed phase inherits the total viscoplastic strain of the parent phase,
- there is no elastic limit in viscoplasticity,
- the problem is restricted to small deformations.

The energy of the displacement problem is formulated as follows:

$$\mathcal{L}^u(\nabla \mathbf{u}, \phi, d) = E^{ext} - E^{el}(\nabla \mathbf{u}, \phi, d) - \Omega^u(\nabla \mathbf{u}, \phi, d), \quad (2)$$

where  $\mathbf{u}$  is the displacement field.  $E^{ext}$ ,  $E^{el}$  and  $\Omega^u$  are respectively the external work, the stored elastic strain energy and the viscoplastic strain energy.

The external work done by the body ( $f_v$ ) and boundary ( $\bar{\mathbf{i}}$ ) forces illustrated in Fig. 3 is given by:

$$E^{ext} = \int_V (f_v \cdot \mathbf{u}) dV + \int_{\partial V} (\bar{\mathbf{i}} \cdot \mathbf{u}) dS. \quad (3)$$

The stored elastic energy is split into tensile ( $\psi_0^+$ ) and compression ( $\psi_0^-$ ) components (Bernard et al., 2012):

$$E^{el}(\nabla \mathbf{u}, \phi, d) = \int_V \psi^{el}(\nabla \mathbf{u}, \phi, d) dV \quad (4)$$

$$\psi^{el}(\nabla \mathbf{u}, \phi, d) = g(d) \psi_0^+(\epsilon^{el}(\nabla \mathbf{u}, \phi)) + \psi_0^-(\epsilon^{el}(\nabla \mathbf{u}, \phi)). \quad (5)$$

The decomposition of the elastic strain energy allows a degradation only in tension.  $g(d)$  is the degradation function:

$$g(d) = (1 - d)^2 + p, \quad (6)$$

where  $p$  is a small number responsible for numerical stability.

The degraded Cauchy stress tensor is then given by :

$$\boldsymbol{\sigma} = g(d) \frac{\partial \psi_0^+}{\partial \boldsymbol{\epsilon}^{el}} + \frac{\partial \psi_0^-}{\partial \boldsymbol{\epsilon}^{el}}, \quad (7)$$

where  $\boldsymbol{\epsilon}^{el}$  is the elastic strain tensor. The degradation function directly acts on the tensile component of the stress tensor.

The total strain field ( $\boldsymbol{\epsilon}$ ) is divided into elastic ( $\boldsymbol{\epsilon}^{el}$ ), viscoplastic ( $\boldsymbol{\epsilon}^{vp}$ ) and eigenstrain ( $\boldsymbol{\epsilon}^*$ ) components:

$$\boldsymbol{\epsilon} = \boldsymbol{\epsilon}^{el} + \boldsymbol{\epsilon}^{vp} + \boldsymbol{\epsilon}^*. \quad (8)$$

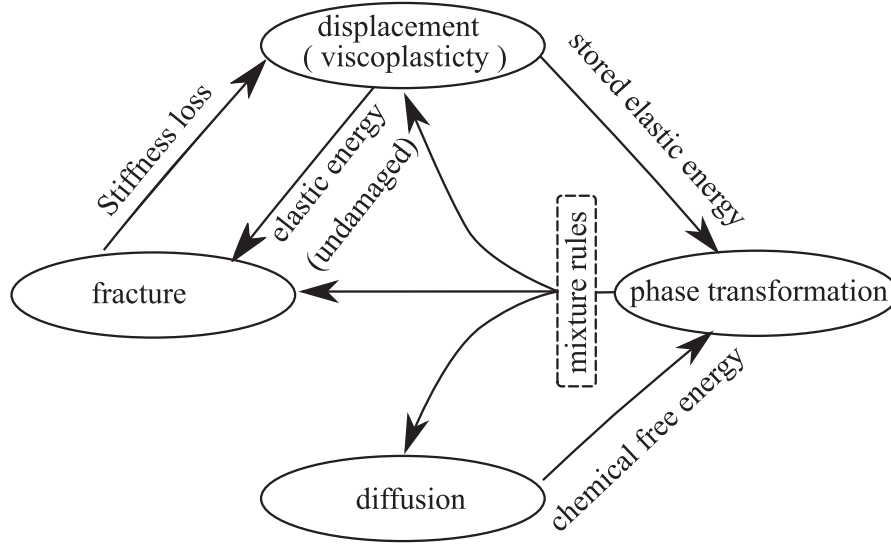


Fig. 2. Overview of the modeled couplings.

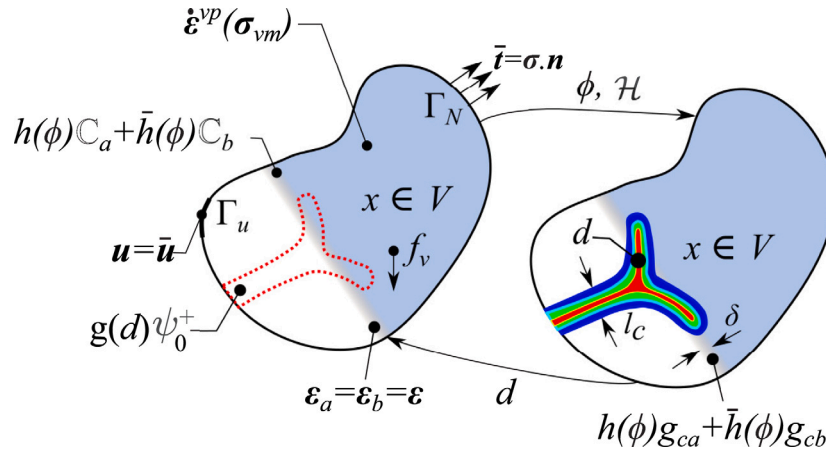


Fig. 3. Illustration of the staggered scheme for solving the fracture and displacement problems in elastoviscoplastic heterogeneous solids.

In this work,  $\epsilon^*$  represents the volumetric change due to the phase transformation. Assuming small deformations, the strain tensor is defined by the symmetric part of the displacement gradient:

$$\epsilon = \nabla^s \mathbf{u}. \quad (9)$$

In the interface, a mixing scheme is applied to determine the effective behavior. Several mixing schemes exist in the literature (Voigt, 1928; Reuss and Angew, 1929; Ammar et al., 2009a; Durga et al., 2013; Mosler et al., 2014; Wang and Khachaturyan, 1995). Voigt's, Reuss's and Khachaturyan's schemes are the most used. For the two former ones, the equivalent elastic strain is calculated from the equivalent compliance tensor. In a damaged region ( $d = 1$ ), this compliance tensor is no longer well defined and tends towards infinity which can therefore induce numerical convergence issues.

Herein, we have retained Khachaturyan's scheme, which does not need this compliance tensor to compute equivalent elastic strain. Therefore, the total strain is assumed to be identical in both coexisting phases while the mixture rules are applied to viscoplastic strain components, eigenstrains and to Lamé parameters ( $\lambda, \mu$ ):

$$\epsilon = \epsilon_a = \epsilon_b, \quad (10)$$

$$\epsilon^{vp}(\nabla \mathbf{u}, \phi) = h(\phi)\epsilon_a^{vp}(\nabla \mathbf{u}) + \bar{h}(\phi)\epsilon_b^{vp}(\nabla \mathbf{u}), \quad (11)$$

$$\epsilon^*(\phi) = h(\phi)\epsilon_a^* + \bar{h}(\phi)\epsilon_b^*, \quad (12)$$

$$\lambda(\phi) = h(\phi)\lambda_a + \bar{h}(\phi)\lambda_b \quad (13.1)$$

$$\mu(\phi) = h(\phi)\mu_a + \bar{h}(\phi)\mu_b. \quad (13.2)$$

The subscripts  $a$  and  $b$  indicate the two coexisting phases. The standard choice of the homogenization function  $h(\phi) = 1 - \bar{h}(\phi)$  is (Wang et al., 1993a):

$$h(\phi) = \phi^2(3 - 2\phi). \quad (14)$$

This mixing scheme, referred to as interpolated scheme by Ammar et al. (2014), assumes that the newly formed phase inherits the total viscoplastic strain of the parent phase in contrast to the homogenization scheme of Voigt (1928) and Reuss and Angew (1929).

The decomposition of elastic energy is given by Bernard et al. (2012):

$$\psi^{el}(\epsilon^{el}, \phi, d) = \mu(\phi) \sum_{i=1}^3 [(\epsilon_i)_-^2 + g(d)(\epsilon_i)_+^2] + \frac{\lambda(\phi)}{2} [g(d)\langle tr(\epsilon) \rangle_+^2 + \langle tr(\epsilon) \rangle_-^2]. \quad (15)$$

For the practical implementation of this decomposition, readers are referred to previous work by Molnár et al. (2020a).

As for the elastic strain energy in Eq. (4), the viscoplastic strain energy is expressed as:

$$\Omega^u(\nabla \mathbf{u}, \phi, d) = \int_V \int_t (\dot{\psi}^{vp}(\nabla \mathbf{u}, \phi, d)) dt dV, \quad (16)$$

$$\dot{\psi}^{vp}(\nabla \mathbf{u}, \phi, d) = \boldsymbol{\sigma}(\nabla \mathbf{u}, d) : \dot{\boldsymbol{\epsilon}}^{vp}(\nabla \mathbf{u}, \phi). \quad (17)$$

The viscoplastic dissipation is calculated from the degraded stress tensor (see Eq. (7)). Since viscoplastic strain does not induce a change in volume, the viscoplastic energy can be simplified according to:

$$\dot{\psi}^{vp}(\nabla \mathbf{u}, \phi) = \sigma_{vm}(d) \dot{\epsilon}_{vm}^{vp}(\nabla \mathbf{u}, \phi), \quad (18)$$

where  $\sigma_{vm}$  and  $\dot{\epsilon}_{vm}^{vp}$  are respectively the von Mises stress and equivalent viscoplastic strain rate. An elastic limit is not integrated into this work. The equivalent viscoplastic strain rate in each of the phases  $a, b$  is described by Norton's law:

$$\dot{\epsilon}_{vm,i}^{vp} = A_i \sigma_{vm}^{n_i}, \quad (19)$$

where  $A_i$  and  $n_i$  are Norton's material parameters. Note that in Eq. (19) the equivalent viscoplastic strain rate in each of the phases is calculated from the equivalent von Mises stress. The rule of mixture used in this work does not give access to the stress tensor of each phase.

By taking the variation of Eq. (2), the corresponding strong form of the displacement problem can be obtained:

$$\delta L^u = 0 \quad \forall \delta \mathbf{u} \rightarrow \nabla \cdot \boldsymbol{\sigma} - \mathbf{f}_v = 0 \text{ in } V, \quad (20.1)$$

$$\boldsymbol{\sigma} \cdot \mathbf{n} = \bar{\mathbf{t}} \quad \text{on } \Gamma_N, \quad (20.2)$$

$$\mathbf{u} = \bar{\mathbf{u}} \quad \text{on } \Gamma_u. \quad (20.3)$$

## 2.2. Fracture problem

The fracture problem is formulated under the following main assumptions:

- the crack surface opening is driven by the tensile elastic (undamaged) strain energy,
- the length scale ( $l_c$  see Fig. 1(b)) is constant in the whole domain,
- the critical energy release rate per unit surface ( $g_c$ ) is treated as a material parameter,
- the damage is irreversible.

The energy functional to solve the crack topology is formulated as follows:

$$\mathcal{L}^d(\nabla \mathbf{u}, \phi, d) = \Omega^d(\phi, d, \nabla d) + T(\phi, d) - E^{el}(\nabla \mathbf{u}, \phi, d), \quad (21)$$

where  $\Omega^d$  is the fracture energy and  $T$  is the threshold function. The regularized phase-field Griffith fracture energy can be expressed as (Bourdin et al., 2000):

$$\Omega^d(\phi, d) = \int_{\Gamma} g_c(\phi) d \Gamma \approx \int_V g_c(\phi) \gamma(d) dV, \quad (22)$$

$$\gamma(d, \nabla d) = \frac{1}{2l_c} d^2 + \frac{l_c}{2} |\nabla d|^2, \quad (23)$$

where  $\gamma$  is the fracture energy density and  $g_c$  the equivalent surface energy needed to create a unit fracture surface and  $l_c$  is the length scale parameter which controls the scale of damage penetration. For details on this approximation, readers are invited to consult previous works of Miehe et al. (2010a) or Molnár and Gravouil (2017).

The work of Molnár et al. (2020a) shows a unique correlation between  $l_c$  and the material's strength, based on the maximum load and the crack topology, which allows us to give the length scale parameter physical meaning. However initially,  $l_c$  is used as a numerical aid. Therefore, the mixture rule is applied only to  $g_c$  but not to  $l_c$ :

$$g_c(\phi) = h(\phi)g_{ca} + \bar{h}(\phi)g_{cb} \quad (24)$$

The threshold function in Eq. (21) is chosen as (Molnár et al., 2020a; Miehe et al., 2016b):

$$T(d) = \int_V [(1 - g(d)) \psi_c(\phi)] dV, \quad (25)$$

$$\text{with } \psi_c(\phi) = \frac{g_c(\phi)}{2l_c}.$$

In practice, to solve the fracture topology, the elastic strain energy in Eq. (21) is replaced by a so-called history field  $\mathcal{H}$  (Miehe et al., 2010a) to prevent crack healing:

$$\mathcal{H}_0 = 0, \quad (26.1)$$

$$\mathcal{H}_{n+1} = \max \left\{ \begin{array}{l} \psi_0^+(\nabla \mathbf{u}, \phi) - \psi_c(\phi) \\ \mathcal{H}_n \end{array} \right\} \quad (26.2)$$

This history field ( $\mathcal{H}$ ) helps to satisfy the Karush–Kuhn–Tucker conditions (Singh et al., 2016). In addition to the introduction of the history field, the damage irreversibility is explicitly enforced in the displacement problem ( $d \geq 0$ ) as there is no mathematical proof that the history field alone is sufficient to ensure damage irreversibility. Therefore, the energy functional to solve the crack topology can be rewritten as:

$$\mathcal{L}^d(\nabla \mathbf{u}, \phi, d) = \Omega^d - \int_V [g(d) \mathcal{H}(\nabla \mathbf{u}, \phi) - \psi_c(\phi)] dV. \quad (27)$$

As for the displacement problem the strong form of fracture topology can be deduced as:

$$\delta \mathcal{L}^d = 0 \quad \forall \delta d \rightarrow \frac{g_c}{l_c} (d - l_c^2 \Delta d) = 2(1 - d) \mathcal{H} \quad \text{in } V, \quad (28.1)$$

$$\nabla d \cdot \mathbf{n} = 0 \quad \text{on } \Gamma, \quad (28.2)$$

## 2.3. Coupled diffusion-phase transformation problem

The coupled problem of diffusion and phase transformation is formulated by assuming that the diffusion of chemical species and the effect of the elastic energy on the phase transformation are isotropic. The starting point for deriving the evolution laws of the diffusion and phase transformation problem is the total free energy functional defined by :

$$\mathcal{L}^{ch}(\nabla \mathbf{u}, c, \phi, d) = \int_V \psi(\nabla \mathbf{u}, c, \phi, d) dV, \quad (29)$$

where  $\psi$  is the Helmholtz free energy density.  $\psi$  is the amount of energy stored in the system per unit volume. Thus,  $\psi$  is made up of the stored elastic strain energy ( $\psi^{el}$ ), the chemical energy ( $\psi^{ch}$ ) and interface energy ( $\psi^{interface}$ ) contributions (de Rancourt et al., 2016):

$$\psi(\nabla \mathbf{u}, c, \phi, d) = \psi^{el}(\nabla \mathbf{u}, \phi, d) + \psi^{ch}(c, \phi) + \psi^{interface}(\phi, \nabla \phi). \quad (30)$$

The viscoplastic energy in Eq. (16) as well as the fracture energy in Eq. (22) are dissipated energies and therefore do not form part of the free energy in Eq. (30). Although the effects of fracture and viscoplasticity do not appear explicitly in Eq. (30), they have an indirect effect through the stored elastic strain energy. Indeed, the energy dissipated by fracture and viscoplasticity comes from the stored elastic energy. By dissipating the stored elastic energy that is part of the free energy, fracture and viscoplasticity contribute indirectly to the coupled diffusion-phase transformation problem.

The equivalent chemical free energy density ( $\psi^{ch}$ ) is obtained by a mixing law on the homogeneous chemical free energy densities of both phases ( $\psi_i^{ch}$ ) (Kim et al., 1998):

$$\psi^{ch}(c, \phi) = h(\phi) \psi_a^{ch}(c) + \bar{h}(\phi) \psi_b^{ch}(c). \quad (31)$$

For the sake of simplicity, the chemical free energy density  $\psi_i^{ch}$  of each phase  $i = \{a, b\}$  is chosen as a square function of the concentration  $c$  (Echebarria et al., 2004):

$$\psi_i^{ch}(c) = \frac{1}{2} k_i (c - c_i)^2, \quad (32)$$

where  $k_i$ , and  $c_i$  are respectively the curvature of the free energy density and the equilibrium concentration of each phase.

The interface contribution  $\psi^{interface}$  is given by Kim et al. (1998):

$$\psi^{interface}(\phi, \nabla\phi) = W g_{ch}(\phi) + \frac{\alpha}{2} \nabla\phi \cdot \nabla\phi, \quad (33)$$

where  $W$  is the height of the energy barrier accounting for the free energy penalty of the interface,  $\alpha$  is the coefficient of the gradient term of the interface energy in Eq. (33) and  $g_{ch}(\phi)$  is the double well potential (Raabe et al., 2004):

$$g_{ch}(\phi) = \phi^2(1 - \phi)^2. \quad (34)$$

Fig. 4 illustrates this Helmholtz free energy density in Eq. (30) without the elastic part. There are two local minima at  $c = c_a$  and  $c = c_b$  which correspond to the equilibrium concentrations of each phase. Fig. 4(b) displays the 2D projection onto the  $(\psi - c)$  plane of the 3D representation in Fig. 4(a). The black curve represents the chemical free energy density of phase  $b$  ( $\phi = 0$ ) and the red curve corresponds to the free energy density of phase  $a$  ( $\phi = 1$ ).

The diffusion and phase transformation problem are governed by the corresponding driving force defined as the functional derivative of the total free energy. We obtain the Cahn–Hilliard equation by deriving the total free energy in Eq. (29) with respect to  $c$ :

$$\frac{\partial c(\mathbf{x}, t)}{\partial t} = \nabla \cdot \left( -L(\phi) \nabla \cdot \left( \frac{\delta F}{\delta c} \right) \right) = \nabla \cdot \left( -L(\phi) \nabla \left( \frac{\partial \psi}{\partial c} \right) \right). \quad (35)$$

The concentration ( $c$ ) is a conserved field for which the spatial average is constant over time. Boundary conditions are used to take into account the exchanges on the edges. In the same way, the Allen–Cahn equation is obtained by deriving the total free energy in Eq. (29) with respect to  $\phi$ . However, the order parameter ( $\phi$ ) is not a conserved field:

$$\frac{\partial \phi(\mathbf{x}, t)}{\partial t} = M \frac{\delta F}{\delta \phi} = M \frac{\partial \psi}{\partial \phi} - \nabla \cdot \frac{\partial \psi}{\partial \nabla \phi}, \quad (36)$$

where  $M$  is the interface mobility parameter which must be as large as possible in the case of diffusion-controlled phase transformation (de Rancourt et al., 2016),  $L(\phi)$  is the homogenized diffusion coefficient (Onsager coefficient) given by Ammar et al. (2009a):

$$L(\phi) = h(\phi) \frac{D_a}{k_a} + \bar{h}(\phi) \frac{D_b}{k_b}, \quad (37)$$

where  $D_i$  is the diffusion coefficient of the phases.  $L(\phi)$  is chosen so as to recover Fick’s law in a homogeneous case. For a homogeneous material ( $\phi = 0$ ), Eq. (35) is equivalent to Fick’s law:

$$\frac{\partial c}{\partial t} = \nabla \cdot \left( -L(0) \nabla \left( \frac{\partial \psi}{\partial c}(0) \right) \right) \quad (38.1)$$

$$= \nabla \cdot \left( -\frac{D_b}{k_b} \nabla (k_b(c - c_b)) \right) \quad (38.2)$$

$$= -D_b \Delta c. \quad (38.3)$$

The interface energy ( $\omega$ ) and the interface thickness ( $\delta$ ) (see Fig. 1) can be deduced from  $\alpha$  and  $W$  by Ammar et al. (2009a), Kim et al. (1998):

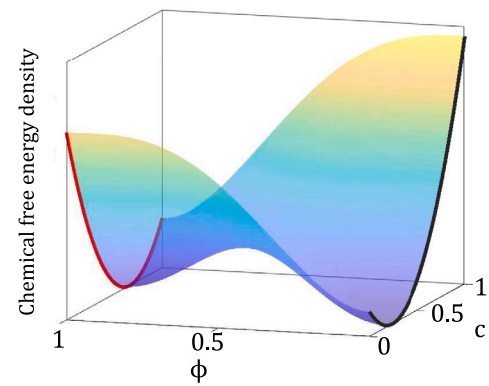
$$\omega = \frac{\sqrt{\alpha W}}{3\sqrt{2}}, \quad (39)$$

$$\delta = \theta \sqrt{\frac{2\alpha}{W}}, \quad (40.1)$$

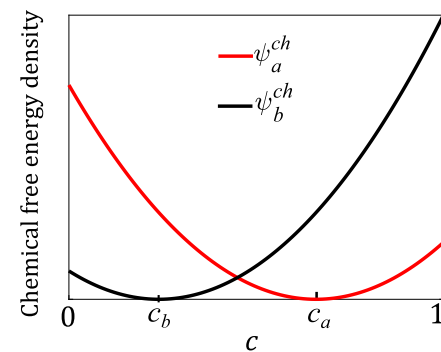
$$\theta = \ln \left( \frac{1 - \eta}{\eta} \right). \quad (40.2)$$

Eq. (40.1) is established assuming that the interface region ranges from  $\phi = \kappa$  to  $\phi = 1 - \kappa$ . In this work,  $\kappa = 0.05$  was chosen.

To be consistent, the model must verify the laws of thermodynamics. A variation in  $g_c$  during a fracture process can compromise the energy balance and thus violate the first principle of thermodynamics.



(a) 3D representation



(b) 2D projection

Fig. 4. Illustration of the chemical free energy density.

This problem is observed in phenomenological phase-field fatigue models (Carrara et al., 2020) and rate-dependent fracture (Yin et al., 2020), where the authors redefined the dissipation rate. Thus the overall fracture surface is no more the measure of dissipated energy in fracture. The criterion  $d > 0$  explicitly imposed can also affect the energy balance if  $g_c$  varies. It is also important to recall that the fracture threshold energy introduced in Eq. (21), which has no real physical basis, can also be considered as a violation of thermodynamic consistency. The second law of thermodynamics is discussed in detail in Appendix A.

#### 2.4. Staggered time-integration algorithm

The proposed model has been implemented in the commercial Abaqus finite element code through a UEL routine. The flowchart in Fig. 5 shows the basic incrementation process. At each increment, the displacement problem, diffusion problem and phase transformation problem are solved together on the basis of the last converged fracture topology and vice versa. A Newton–Raphson method can be used to solve the global problem iteratively:

$$\begin{bmatrix} \mathbf{K}_{uu} & \mathbf{K}_{u\phi} & \mathbf{0} & \mathbf{0} \\ \mathbf{K}_{\phi u} & \mathbf{K}_{\phi\phi} & \mathbf{K}_{\phi c} & \mathbf{0} \\ \mathbf{0} & \mathbf{K}_{c\phi} & \mathbf{K}_{cc} & \mathbf{0} \\ \mathbf{0} & \mathbf{0} & \mathbf{0} & \mathbf{K}_{dd} \end{bmatrix} \begin{bmatrix} \mathbf{u}_{n+1} \\ \phi_{n+1} \\ c_{n+1} \\ \mathbf{d}_{n+1} \end{bmatrix} = - \begin{bmatrix} \mathbf{r}_n^u \\ \mathbf{r}_n^\phi \\ \mathbf{r}_n^c \\ \mathbf{r}_n^d \end{bmatrix}, \quad (41)$$

where,  $\mathbf{K}_{ij}$  are elementary stiffness matrices,  $\mathbf{u}_{n+1}$ ,  $c_{n+1}$ ,  $\phi_{n+1}$  and  $\mathbf{d}_{n+1}$  are the new nodal solutions at  $t_{n+1}$ .  $\mathbf{r}_n^u$ ,  $\mathbf{r}_n^c$ ,  $\mathbf{r}_n^\phi$  and  $\mathbf{r}_n^d$  are residues. The finite element formulation of the present model is detailed in Appendix B.

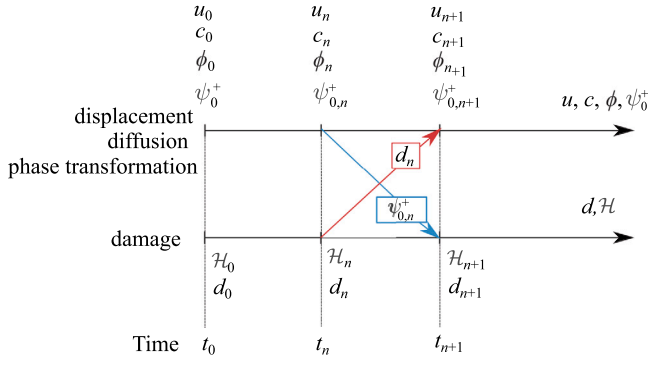


Fig. 5. Flowchart of the staggered algorithm used to solve the multi-physics problem in Abaqus.

Cracking and viscoplasticity do not occur on the same time scale. Therefore, an adaptive time step control is required to make the simulation computationally feasible. The time step was automatically controlled by the local tensile elastic strain energy increment:

$$dH \leq \eta \psi_c. \quad (42)$$

This allows the time step to be increased until crack initiation is reached. In the case of unstable crack propagation, the local tensile elastic strain energy at the crack tip becomes independent of the time step which is then reduced to a minimum value of  $dt = 10^{-9}$  s. This way, the unstable crack propagation is detected precisely. More details on this automatic time step control based on the energy constraint can be found in [Molnár et al. \(2020b\)](#).

### 2.5. Model testing strategy

The implemented model is tested by examining quantities that describe the fracture response of a structure. As shown in [Fig. 6](#), the critical load ( $\sigma^c$ ) is defined as the maximum amount of tensile stress that the material can withstand before failure. The energy density until failure ( $U_t$ ) gives an indication of the toughness of a structure.  $U_t$  represents the area below the stress-strain curve:

$$U_t = \int_0^{\epsilon_f} \sigma d\epsilon, \quad (43)$$

where  $\epsilon_f$  is the strain at failure. A Brittle Response (BR) represents a behavior characterized by a high value of  $\sigma^c$  and a low value of  $U_t$ , while Ductile Response (DR) is a behavior characterized by a low value of  $\sigma^c$  and a high value of  $U_t$ .

### 3. Examples and results

This section analyzes the effect of viscoplasticity and diffusive phase transformation on the critical load, energy density until failure and crack topology using examples of increasing complexity. In [Section 3.1](#), it is shown that the proposed model is able to simulate some well-known behaviors for viscoplastic solids, such as ductile failure at low strain rates and brittle failure at high strain rates. The role of viscoplasticity at the crack tip is also highlighted in the case of the simple extension (mode I). From [Section 3.2](#) to [Section 3.4](#), the model is exploited to study the fracture behavior in a heterogeneous solid. The case of a rigid layer growing on a soft matrix is discussed in [Section 3.2](#). The effect of phase transformations and the internal stresses they generate are illustrated. [Section 3.3](#) deals with the fracture behavior of a heterogeneous solid consisting of an inclusion evolving in a matrix. The effect of the stiffness ratio between the inclusion and the matrix on the crack topology is presented. The case of several randomly distributed inclusions in the matrix is treated in [Section 3.4](#).

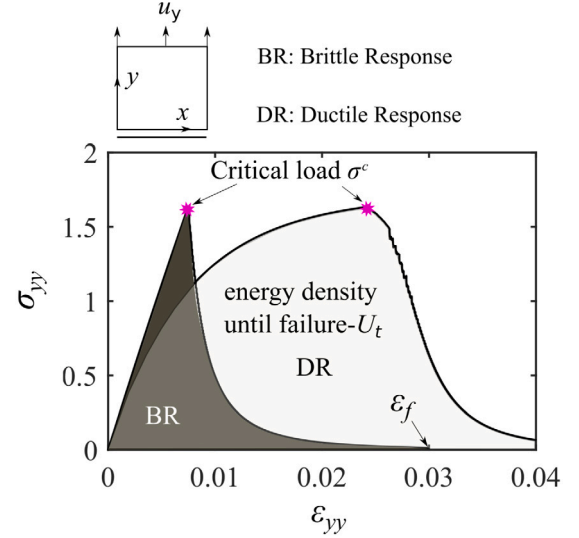


Fig. 6. Stress-strain curves for Brittle Response (BR) and Ductile Response (DR).

Table 1

Definitions of the dimensionless parameters.

Physical	Dimensionless
Length: $l$ [m]	$\tilde{l} = \frac{l}{L}$
Times: $t$ [s]	$\tilde{t} = \frac{t}{\tau}$
Mechanical properties ( $n$ is the Norton's exponent)	
Young's modulus: $E$ [Pa]	$\tilde{E} = \frac{E}{E_d}$
Norton's constant: $A$ [ $J^{-n} m^{3n} s^{-1}$ ]	$\tilde{A} = A \cdot E_d^n \cdot \tau$
Fracture surface energy: $g_c$ [ $J m^{-2}$ ]	$\tilde{g}_c = \frac{g_c}{E_d \cdot L}$
Fracture length scale: $l_c$ [m]	$\tilde{l}_c = \frac{l_c}{L}$
Chemical properties	
Concentration: $c$	$\tilde{c} = \frac{c}{c_a - c_b}$
Interface energy: $\omega$ [ $J m^{-2}$ ]	$\tilde{\omega} = \frac{\omega}{E_d \cdot L}$
Interface thickness: $\delta$ [m]	$\tilde{\delta} = \frac{\delta}{L}$
Interface mobility: $M$ [ $J^{-1} m^3 s^{-1}$ ]	$\tilde{M} = M \cdot E_d \cdot \tau$
Diffusivity: $D$ [ $m^2 s^{-1}$ ]	$\tilde{D} = \frac{D \cdot \tau}{L^2}$
Chemical free energy curvature: $k$ [ $J m^{-3}$ ]	$\tilde{k} = \frac{k}{E_d}$

Parameters used for the simulations are dimensionless so that the results can be extrapolated to other sets of parameters. The length, time and energy density scales are defined respectively by the size of the system  $L$ , the characteristic diffusion time  $\tau = L^2/\max(D_i)$  and the chemical free energy density curvature  $E_d = \beta \min(k_i)$ . Here,  $\beta$  is an arbitrary positive constant. The concentrations are also scaled by the difference between the equilibrium concentrations ( $c_a - c_b$ ) of the two phases ([de Rancourt et al., 2016](#)). Parameters to be scaled, denoted with tildes, are summarized in [Table 1](#).

All presented results are dimensionless but for the sake of clarity the tilde symbol has been omitted. The simulations are carried out under plane strain conditions.

#### 3.1. Competition between fracture and viscoplasticity

The proposed phase-field model does not explicitly predict a coupling between fracture and viscoplasticity. However, these two phenomena are indirectly linked through the elastic strain energy in [Eq. \(4\)](#) that can be dissipated either by cracking or by viscoplasticity.

### 3.1.1. Homogeneous solution

A single 2D homogeneous plane strain element is the simplest case, where the interaction between fracture and viscoplasticity can be understood. A square plate with dimensions of  $1 \times 1$  is subjected to a simple shear strain rate by moving its top side in the  $x$  direction while its bottom side is fixed in both  $x$  and  $y$  directions. Young's modulus was set to  $E = 210$  with  $\nu = 0.3$ ,  $g_c = 2 \times 10^{-3}$  and  $l_c = 2 \times 10^{-4}$ . The energy increment constraint in Eq. (42) was set to  $\eta = 1\%$ . Only cracking and viscoplasticity are considered in this example.

Regardless of cracking, the viscoplastic problem can be solved analytically. By combining Eqs. (7) and (15) which allow to calculate the stress with Norton's law in Eq. (18) in the case of a pure shear in a homogeneous solid, we obtain the following differential scalar equation:

$$\dot{\tau}_{xy} = \mu \left( \dot{\gamma}_{xy} - A(\sqrt{3})^{n+1} \tau_{xy}^n \right), \quad (44)$$

where  $\mu = \frac{E}{2(1+\nu)}$  is the shear modulus. The steady shear stress ( $\tau_{xy}^\infty$ ) described by  $\dot{\tau}_{xy} = 0$  can be deduced from Eq. (44) by:

$$\tau_{xy}^\infty = 3^{-\frac{n+1}{2n}} \cdot \left( \frac{\dot{\gamma}_{xy}}{A} \right)^{\frac{1}{n}}, \quad (45)$$

the corresponding steady stored tensile elastic strain energy ( $\psi^\infty$ ) is given by:

$$\psi^\infty = \frac{(\tau_{xy}^\infty)^2}{4\mu}. \quad (46)$$

It becomes apparent from Eq. (45) that the viscoplastic behavior is only dependent on the ratio  $[\dot{\gamma}_{xy}/A]$ , and not on absolute values. This remains the case when fracture is taken into account, regardless of the loading conditions.

To reach the failure of the element, the steady tensile elastic strain energy ( $\psi^\infty$ ) must be greater than the fracture threshold ( $\psi_c$ ). Therefore, the threshold ratio ( $[\dot{\gamma}_{xy}/A]^c$ ) required to reach this fracture threshold is given by:

$$\psi^\infty \geq \psi_c \Rightarrow [\dot{\gamma}_{xy}/A]^c = \sqrt{3} \left( \frac{6\mu g_c}{l_c} \right)^{\frac{n}{2}}. \quad (47)$$

For  $n = 1$ , the global solution of Eq. (44) is trivial and the tensile ( $\psi_{0,+}^{el}$ ) component of elastic energy can be calculated as:

$$\psi_{0,+}^{el} = \psi^\infty \left[ 1 - \exp\left(-\frac{\mu \gamma_{xy}}{\tau_{xy}^\infty}\right) \right]^2. \quad (48)$$

In Fig. 7, it can be seen that for  $[\dot{\gamma}_{xy}/A] \leq [\dot{\gamma}_{xy}/A]^c$  the purely viscoplastic analytical solution (red continuous line) given by Eq. (48) is consistent with the numerical phase-field solution. The steady tensile elastic energy does not exceed the fracture threshold ( $\psi_c$ ). The viscoplastic dissipation rate is high enough to keep the tensile elastic energy below the fracture threshold. For  $[\dot{\gamma}_{xy}/A] = 1.3[\dot{\gamma}_{xy}/A]^c$ , the viscoplastic dissipation rate is no longer high enough. The material cracks as soon as the fracture threshold is reached ( $\psi_+^{el}/\psi_c = 1$ ) and the total elastic strain energy is dissipated. These results highlight the role of the fracture threshold ( $\psi_c$ ) introduced in the fracture energy description. Two time scales can be observed for the elastic strain energy dissipation rate. Damage occurs on a very short time scale, leading to the dissipation of the total elastic energy ( $\psi_+^{el} \rightarrow 0$ ), while viscoplasticity occurs on a longer time scale, leading to non-zero elastic strain energy at equilibrium ( $\psi_+^{el} \rightarrow \psi^\infty$ ).

A dichotomous search procedure is used to numerically determine the critical shear  $[\dot{\gamma}_{xy}/A]^c$  and tensile  $[\dot{\epsilon}_{yy}/A]^c$  ratios required to reach the fracture threshold. Starting from a large interval in which the ratio is expected, we progressively reduce it (depending on whether the failure of the element is reached or not) until the size of the interval is less than 1% of its central value.

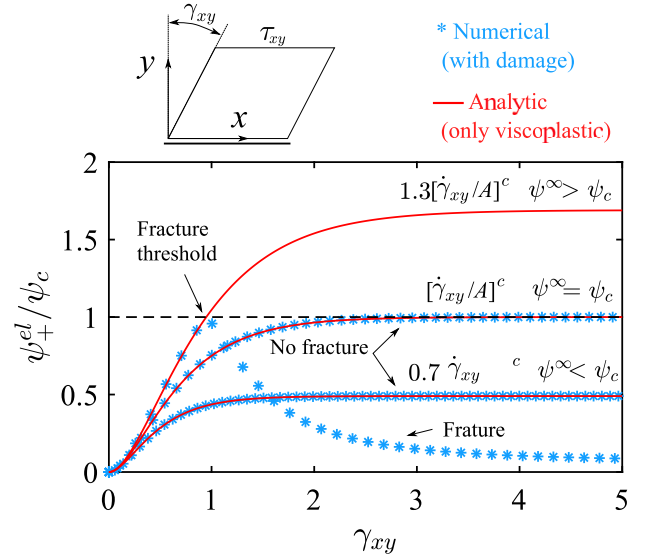


Fig. 7. Normalized tensile elastic strain energy as a function of the ratio  $[\dot{\gamma}_{xy}/A]^c$ . Norton's exponent was set to  $n = 1$  for comparison with the analytical solution given by Eq. (48).

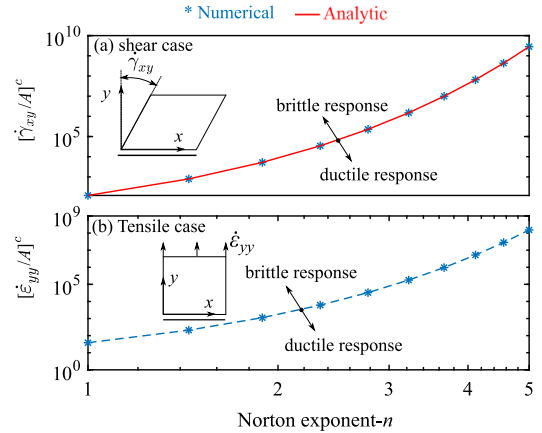


Fig. 8. Transition between brittle and ductile response as a function of Norton's exponent ( $n$ ). In the shear case (a) the numerical solution is compared with the analytical solution given by Eq. (47). In the tensile case (b), only the numerical solution is shown because there is no explicit analytical solution.

To change the ratio, we vary the applied strain rate and keep Norton's constant ( $A$ ) unchanged.

Fig. 8(a) and (b) respectively show the evolution of the threshold shear  $[\dot{\gamma}_{xy}/A]^c$  and tensile  $[\dot{\epsilon}_{yy}/A]^c$  ratios as a function of Norton's exponent ( $n$ ). In the shear case, the analytical solution (red continuous line) given by Eq. (47) is consistent with its numerical counterpart. The critical shear and tensile ratios increase exponentially with Norton's exponent. For a ratio less than the critical value, viscoplasticity dominates the material's behavior and fracture is not observed. By increasing the ratio, the response becomes more and more brittle and fracture appears when the critical ratio is reached.

This first case provided a deeper understanding of the interaction between fracture and viscoplasticity in the proposed model.

### 3.1.2. Mode I: Tensile opening

The mode I tensile opening test is used to analyze the effect of viscoplasticity on the fracture behavior. Fig. 9(a) illustrates the problem. The material is homogeneous and only fracture and viscoplasticity are considered. Symmetry boundary conditions make it possible to reduce

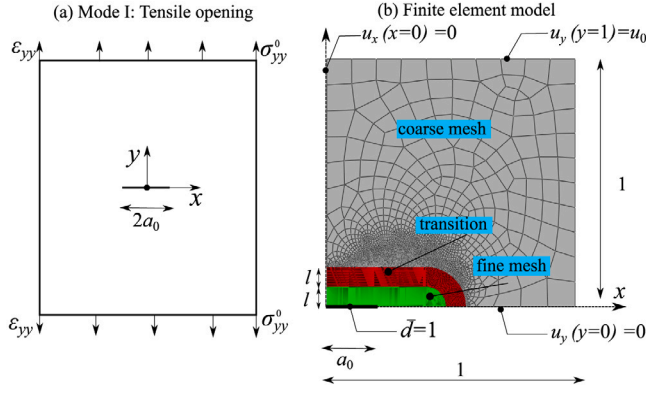


Fig. 9. Mode I tensile opening: (a) schematic problem; (b) double symmetry finite element model.  $a_0 < 10^{-2}$  to avoid a significant size effect. For the phase-field calculation, only the intact horizontal part was constrained against  $y$ , whereas the crack faces were left free to move.

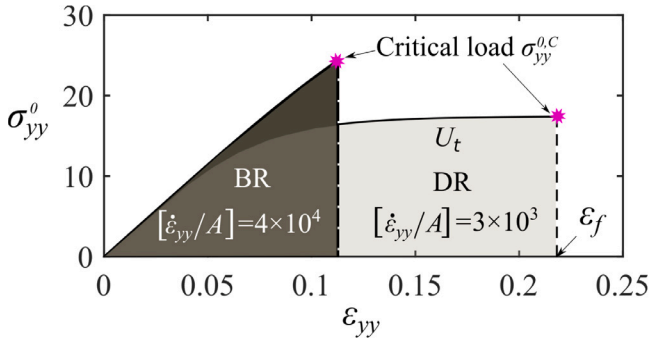


Fig. 10. Stress-strain curves for brittle response (BR) and ductile response (DR) in the case of tensile opening (mode I). The results were obtained with  $a_0 = l_c, n = 3$ .

the problem to a quarter of the geometry Fig. 9(b). The initial crack surface is defined by a Dirichlet boundary condition  $d = 1$  and is left free to move. To avoid any significant size effect, the initial crack length is limited to  $a_0 < 10^{-2}$ . Young's modulus was set to  $E = 210$  with  $\nu = 0.3$ ,  $g_c = 2 \times 10^{-3}$  and  $l_c = 2 \times 10^{-4}$ . The region near the initial crack is finely meshed with a maximum element size of  $h = l_c/10$  to improve the precision of the simulations and reduce the effect of spatial mesh on the results (Molnár et al., 2020a).  $\eta = 50\%$  is sufficient to ensure good convergence of the simulation in this case.

Fig. 10 shows the stress-strain curve until fracture for a ratio of  $[\dot{\epsilon}_{yy}/A] = 3 \times 10^3$  and  $[\dot{\epsilon}_{yy}/A] = 4 \times 10^4$ . Norton's exponent and the initial crack length were respectively set to  $n = 3$  and  $a_0 = l_c$ . For  $[\dot{\epsilon}_{yy}/A] = 3 \times 10^3$ , a Brittle Response (BR) characterized by a high critical load ( $\sigma_{yy}^{0,c}$ ) and a low energy density until failure ( $U_t$ ) is observed, whereas for  $[\dot{\epsilon}_{yy}/A] = 4 \times 10^4$  a Ductile Response (DR) characterized by a low  $\sigma_{yy}^{0,c}$  and a high  $U_t$  is observed.

Fig. 11(a) and (b) respectively show the evolution of  $\sigma_{yy}^{0,c}$  and  $U_t$  as a function of the ratio  $[\dot{\epsilon}_{yy}/A]$  for  $a_0 = l_c$  and  $n = \{1, 3\}$ . By increasing the ratio  $[\dot{\epsilon}_{yy}/A]$ ,  $\sigma_{yy}^{0,c}$  increases but  $U_t$  decreases. This result is consistent with experimental observations (Verleysen and Peirs, 2017). For a high  $[\dot{\epsilon}_{yy}/A]$  ratio,  $\sigma_{yy}^{0,c}$  converges to the critical load ( $\sigma_{yy}^{el,0,c}$ ) and  $U_t$  to the energy density until failure ( $U_t^{el}$ ) in the case of an elastic brittle material. These results show that when the viscoplastic strain rate ( $\dot{\epsilon}^{vp}(A)$ ) is comparable to the applied strain rate ( $\dot{\epsilon}_{yy}$ ), DR is observed because the material undergoes viscoplastic strain and absorbs significant energy before fracture. However, if the viscoplastic strain rate is small compared to the applied strain rate, a BR is observed. The material does not have enough time to dissipate the energy through viscoplastic activity.

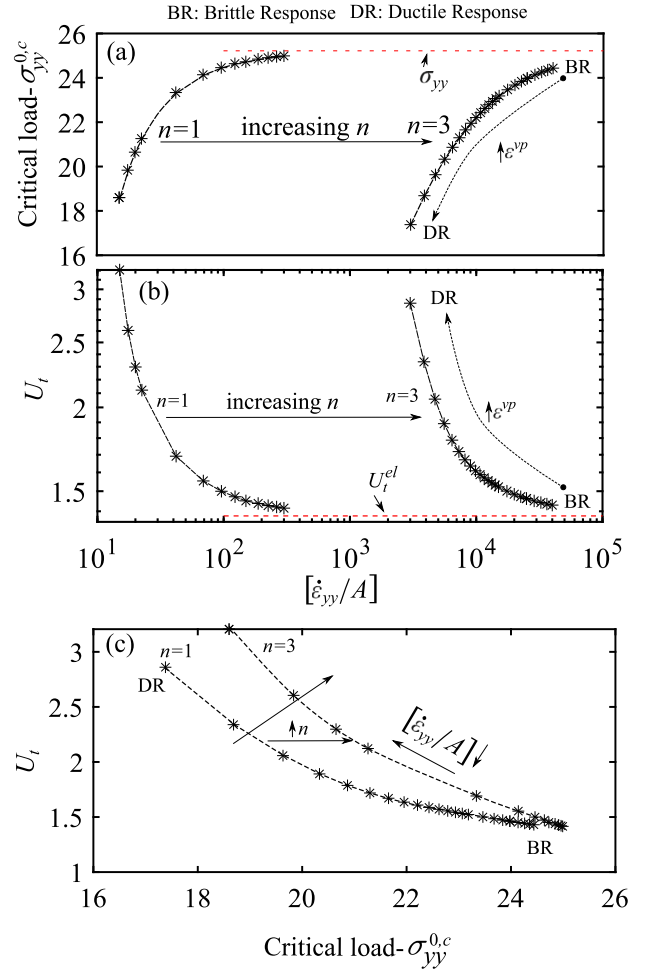


Fig. 11. Critical load (a) and energy density until failure (b) as function of the ratio  $[\dot{\epsilon}_{yy}/A]$ . The critical load ( $\sigma_{yy}^{0,c}$ ) and the energy density until failure ( $U_t^{el}$ ) in the case of an elastic brittle material are also shown. The direction of the increase in viscoplastic strain ( $\epsilon^{vp}$ ) at the crack tip is illustrated. (c) Correlation between the critical load and the energy density until failure. For all simulations, the initial crack length was set to  $a_0 = l_c$ .

The correlation between  $\sigma_{yy}^{0,c}$  and  $U_t$  is shown in Fig. 11(c). For a given Norton's exponent ( $n$ ),  $\sigma_{yy}^{0,c}$  increases as  $U_t$  decreases. Interestingly, it can be seen that by acting simultaneously on Norton's exponent ( $n$ ) and on Norton's constant ( $A$ ), both  $\sigma_{yy}^{0,c}$  and  $U_t$  can be improved.

The critical load as a function of the normalized initial crack length is shown in Fig. 12. The elastic (red circle symbol) and viscoplastic (black star symbol) cases are represented. In the elastic case ( $A = 0$ ), for  $a_0 \gg l_c$ ,  $\sigma_{yy}^{0,c}$  varies linearly with  $a_0$  in log-log scale. This result is consistent with the original Griffith's solution. When  $a_0$  is smaller than  $l_c$ ,  $\sigma_{yy}^{0,c}$  converges to a plateau. This result is similar to that of Molnár et al. (2020a) and is consistent with the size effect found experimentally (Bažant, 1984). This means that the length scale ( $l_c$ ) introduced in the fracture phase-field approach does not spoil the original Griffith's description. In the viscoplastic cases, by increasing the ratio  $[\dot{\epsilon}_{yy}/A]$ , the viscoplastic solution converges to its elastic counterpart. By reducing the ratio  $[\dot{\epsilon}_{yy}/A]$ , viscoplasticity dominates the material's behavior and the effect of the initial crack tends to disappear. The viscoplastic activity at the crack tip mitigates the effect of the initial crack.

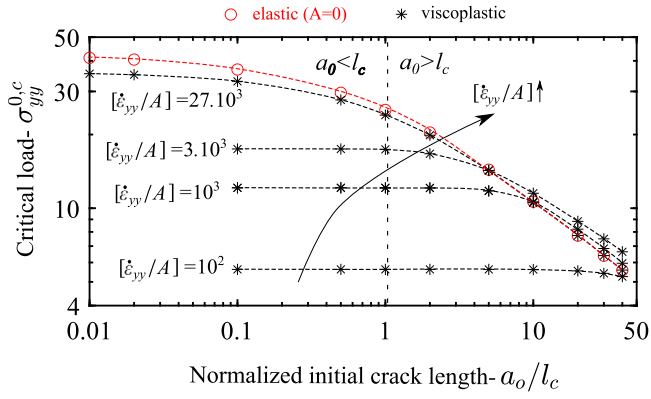


Fig. 12. Critical load obtained by phase-field simulations as function of the initial crack length ( $a_0$ ) normalized by  $l_c$ ; Norton's exponent was set to  $n = 3$  for viscoplastic cases.

### 3.2. Effect of residual stresses on the interaction between fracture and phase transformation

During the growth of an oxide layer, which is the phase formed during the transformation of an alloy, two major phenomena can influence its fracture behavior. These are the induced residual stresses and the evolution of the effective properties of the alloy.

#### 3.2.1. Effect of residual stresses on the fracture behavior: homogeneous solution

During the growth of an oxide layer in an alloy, residual stresses can be induced by the growth strain of the oxide layer. This growth strain may be due to the incompatibility of the molar volumes between the newly formed phase and the parent phase (Panicaud et al., 2006). The growth strain is modeled by an additional eigenstrain ( $\epsilon^*$ ). The effect of this eigenstrain on the fracture behavior can be understood by a single homogeneous elastic 2D plane strain element. A square plate with dimensions of  $1 \times 1$  is subjected to a simple vertical tensile load. Young's modulus was set to  $E = 210$  with  $\nu = 0.3$ ,  $g_c = 2 \times 10^{-3}$  and  $l_c = 2 \times 10^{-2}$ . The energy increment constraint was set to  $\eta = 1\%$ . A planar eigenstrain is embedded within the element  $\epsilon^* = \epsilon^* \delta_{ij}$ , where  $\delta_{ij}$  is the 2nd order identity tensor.

Fig. 13(a) and (b) show respectively the evolution of the normalized tensile elastic strain energy ( $\psi_+^{el}$ ) and the corresponding stress as a function of the applied strain ( $\epsilon_{yy}$ ). The reference case ( $\epsilon^* = 0$ ) and the elastic case ( $\epsilon^* = 0.01$ ) are portrayed. For the latter, it can be seen that the material remains in compression as long as  $\epsilon_{yy} < \epsilon^*$  and the corresponding tensile elastic strain energy which controls the fracture remains at zero. When  $\epsilon_{yy} > \epsilon^*$ , the material goes into tension and tensile elastic strain energy starts to increase.  $\epsilon^*$  does not change the critical load compared to the reference case, but induces an offset on the critical strain. Using the fracture criterion and the stress-strain relation, the critical load ( $\sigma_{yy}^{c,homo}$ ) for this homogeneous case can be obtained by the following equation:

$$\sigma_{yy}^{c,homo} = \left( \frac{2\lambda\mu}{\lambda + 2\mu} + 2\mu \right) \sqrt{\frac{\Psi_c}{2\lambda\mu^2} + \mu}, \quad (49)$$

where  $\lambda = \frac{E\nu}{(1+\nu)(1-2\nu)}$ ,  $\mu = \frac{E}{2(1+\nu)}$  are Lamé's parameters.

As highlighted in Fig. 13(b), compared to the reference case, the elastic case induces an improvement of  $U_t$  corresponding to the energy density in compression that does not contribute to fracture.

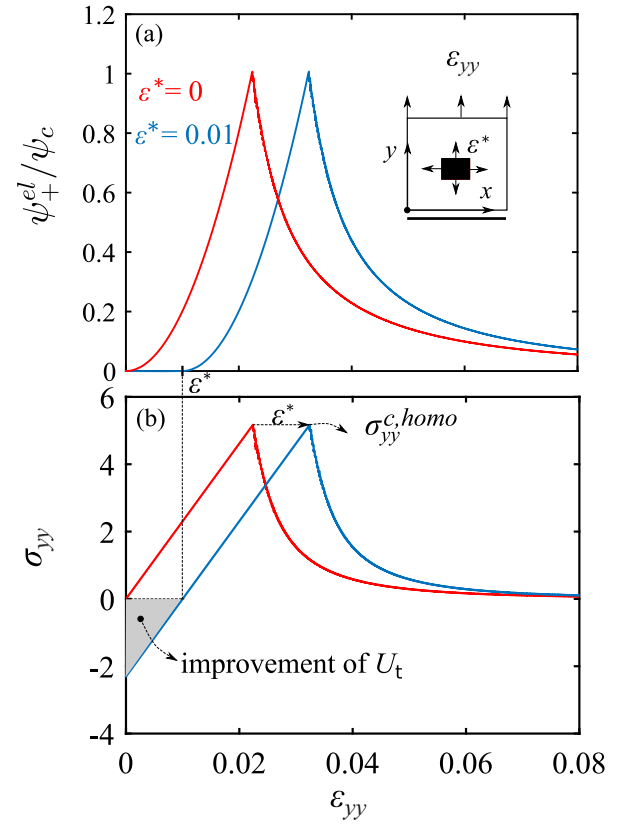


Fig. 13. (a) Normalized tensile elastic strain energy and (b) stress as a function of the applied tensile strain  $\epsilon_{yy}$ . The reference case ( $\epsilon^* = 0$ ) and the elastic case ( $\epsilon^* = 0.01$ ) are shown.

#### 3.2.2. Heterogeneous case with planar interface

This section investigates the influence of the growth of a misfitting oxide layer ( $\epsilon^*$ ) on its fracture behavior. We proceed in two steps. (i) first, an oxide layer is generated in a matrix under stress-free conditions. Despite such conditions, due to the oxide layer growth strain, the local stress in the oxide layer and matrix are non zero during this growth step. (ii) Second, a macroscopic mechanical load is applied at high rate until failure of the previously formed oxide layer (loading step). The effect of internal stresses on growth kinetics has already been studied by de Rancourt et al. (2016) and Ammar et al. (2014). In this example the mechanical contribution to the growth kinetics is neglected. This is done by choosing the parameters  $k_i$  large enough. The illustration of the mechanical problem combined with the chemical problem is depicted in Fig. 14. An equilibrium hyperbolic tangent-like shape is used to set the initial structure:

$$\phi(x, t = 0) = \frac{1}{2} \left[ 1 - \tanh \left( \frac{\theta(x - f_o)}{\delta} \right) \right], \quad (50)$$

$\theta$  is given by Eq. (40.2) and  $\delta$  refer to the interface thickness,  $f_o = 2 \times \delta$  is the initial fraction of the oxide layer ( $\phi = 1$ ). The matrix is initially in chemical equilibrium ( $c = c_m = 0$ ) and a linear gradient is prescribed within the oxide layer. The oxide layer growth is therefore due to the supersaturation prescribed by the Dirichlet condition ( $c = 1.6$ , note that  $c$  is the normalized concentration, therefore its value can exceed 1) on the left side. During the loading step, the mechanical load is applied using a multi-point constraint (MPC) approach as shown in Fig. 14. The average stress corresponding to the force applied to the top face is given by:

$$\langle \sigma_{yy} \rangle = \frac{1}{L} \int \sigma_{yy} dx. \quad (51)$$

**Table 2**

Dimensionless material parameters used for the simulation of the growth of a misfitting rigid oxide layer on a soft matrix. The subscripts  $o, m$  refer to the oxide layer ( $\phi = 1$ ) and the matrix ( $\phi = 0$ ), respectively.

Elasticity:	$E_m$	58
	$E_o$	210
	$\nu_m = \nu_o = \nu$	0.3
	$\epsilon^*$	0.01
Viscoplasticity:	$n_m = n_o$	3
Fracture:	$g_m = 500 \times g_o$	1.
	$l_c$	$2 \times 10^{-2}$
Chemical:	$\omega$	$2 \times 10^1$
	$\delta$	0.01
	$M$	$10^6$
	$D_m = D_o$	1
	$c_m$	0.
	$c_o$	1.
	$k_m = k_o$	$10^5$

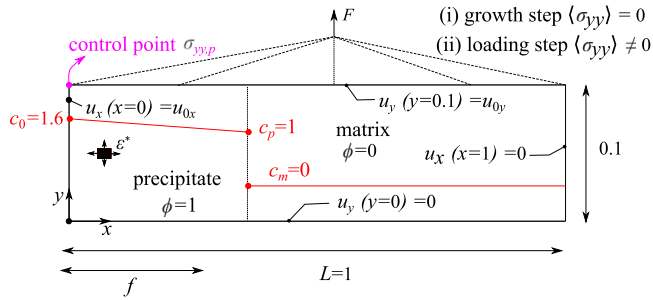


**Fig. 14.** Growth of a rigid misfitting oxide layer in a soft matrix. A multi-point constraint (MPC) is applied to the top and left surfaces to enforce them to remain flat. Simulations are carried out in two steps. (i) Firstly, the oxide layer grows without external applied stress ( $F = 0$ ). (ii) Secondly, a macroscopic mechanical load is applied ( $F \neq 0$ ). The initial concentration is highlighted in red.

$L = 1$  is the system size,  $\langle \sigma_{yy} \rangle$  is applied with a sufficiently high rate compared to the viscoplastic strain rate and the oxide layer growth kinetics. This avoids growth of the oxide layer and viscoplastic activity during the loading step.

The material parameters used for the computation are summarized in Table 2.  $g_c$  of the matrix is set 500 times higher than that of the oxide layer.

The system is meshed with 1000 linear quadrangular elements in the  $x$  direction and 1 element in the  $y$  direction. Ten elements in the interface are sufficient to resolve the interface (de Rancourt et al., 2016). Regarding the time step control, the energy constraint of  $\eta = 1\%$  is needed during the loading step to ensure good accuracy of the simulations.

Fig. 15 depicts the stress profile during the growth of the oxide layer for the reference ( $\epsilon^* = A_o = A_m = 0$ ), elastic ( $\epsilon^* = 0.01, A_o = A_m = 0$ ) and viscoplastic ( $\epsilon^* = 0.01, A_o = A_m = 1$ ) cases. The oxide layer/matrix interface is indicated by the vertical dotted line. In the elastic case the stress remains homogeneous in both matrix and oxide layer while a gradient with high compressive stresses at the interface is observed in the oxide layer in the viscoplastic case. This stress gradient obtained by simulation is consistent with experimental observations (Godlewski et al., 2000; Ly et al., 2011) and is due to the interplay between stress relaxation effects and oxide layer growth. The oxide layer that has been present for a longer period of time has had more time than the newly formed oxide layer to relax the stresses.

In the reference case there is obviously no stress generated during the growth step. The position of the matrix/oxide layer interface in the elastic and viscoplastic cases coincides, indicating a negligible effect of internal stresses on growth kinetics.

Fig. 16(a) illustrates the growth kinetics of the oxide layer (in semi-log scale) during the growth step. As expected for diffusion-controlled

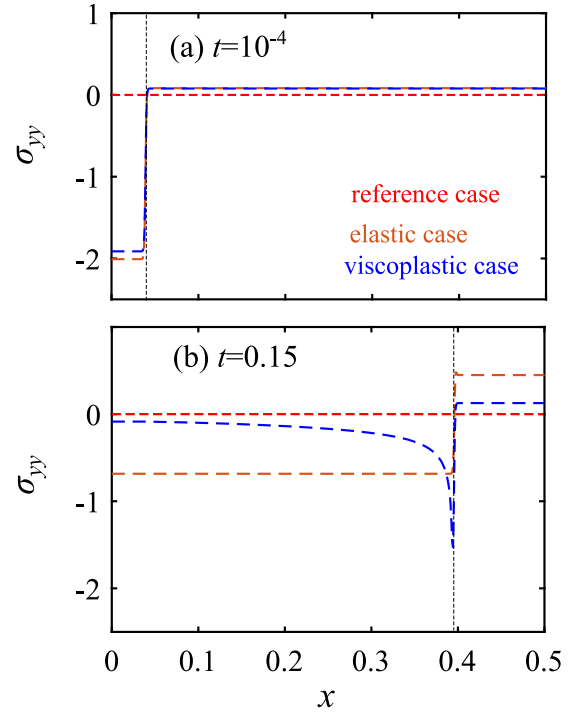


**Fig. 15.** Stress profile associated with the growth of the oxide layer at  $t = 10^{-4}$  (a) and  $t = 0.15$  (b). The reference ( $\epsilon^* = A_o = A_m = 0$ ), elastic ( $\epsilon^* = 0.01, A_o = A_m = 0$ ) and viscoplastic ( $\epsilon^* = 0.01, A_o = A_m = 1$ ) cases are represented. The matrix/oxide layer interface region is indicated by the vertical black dotted line.

processes the kinetics follow a square-root law ( $f = \sqrt{Kt}$ ).  $K = 1.02$  corresponds to the best fit of the data by least square methods. The kinetics is the same in the reference, elastic and viscoplastic cases because as mentioned above, the material parameters are chosen in such a way that the internal stresses do not have any impact on the growth kinetics.

The evolution of the residual stress ( $\sigma_{yy}^r$ ) in the oxide layer (extracted at the defined control point shown in Fig. 14) as a function of the duration of the growth step is illustrated in Fig. 16(b) for the reference, elastic and viscoplastic cases. In the elastic case, during the growth of the oxide layer, the residual compressive stress in the oxide layer is progressively relaxed and tends towards zero when the matrix is fully transformed ( $f = 1$ ). In the viscoplastic case, the stress relaxation is accelerated by the viscoplastic activity. There is obviously no residual stress in the reference case.

Fig. 16(c) compares the critical load ( $\langle \sigma_{yy}^c \rangle$ ) as a function of the duration of the growth step for the three studied cases. The critical load presented here is related to the oxide layer failure. It can be seen that the critical load increases in all cases as the oxide layer grows. The growth of the oxide layer stiffens the alloy and leads to an improvement of the critical load. When  $f = 1$  the homogeneous solution (see Eq. (49)) is reached.

For a given oxide layer fraction, the critical stress is maximal in the elastic case and minimal in the reference case. This shows a beneficial effect of the compressive stresses induced in the oxide layer during its growth. In the viscoplastic case, the critical load curve shifts progressively from the elastic case to the reference case. This is due to the progressive relaxation of the oxide layer residual stress ( $\sigma_{yy}^r$ ) during the growth of the oxide layer. Compared to the reference case, the improvement of the critical load in the elastic or viscoplastic case corresponds to the load required to compensate the compressive stress in the oxide layer.

As shown in Fig. 16(d) the observations made for the critical load are also valid for  $U_l$ .

Similar simulations were carried out by applying a monotonic mechanical load during the growth step. The load is applied with a low rate so that the oxide layer has sufficient time to grow before its failure. The prescribed stress varies linearly from  $\langle \sigma_{yy} \rangle = 0$  at  $t = 0$  to  $\langle \sigma_{yy} \rangle = 16$  at  $t = 1$ .

Fig. 17 shows the stress–strain curve at the control point in the elastic and viscoplastic cases. In the elastic case the stiffening induced by the growth of the oxide layer improves the critical stress. In the viscoplastic case the stiffening is observed at the beginning of the curve after which the softening effect due to the viscoplastic activity progressively takes the lead. The critical strain is thus improved at the expense of the critical stress. The time dependence of the oxide layer growth is given by a square-root law ( $f = \sqrt{Kt}$ ) while that of the viscoplastic strain is given by a power law ( $\epsilon^{vp} = Qt^n$ ,  $n \geq 1$ ). This is why the softening effect of viscoplastic activity, necessarily becomes dominant over the stiffening effect of oxide layer growth.

### 3.3. Heterogeneous case with non planar interface : single inclusion

In this section, the interplay between fracture and morphological evolutions during the diffusion-controlled growth of a single inclusion is investigated. As in the previous section, we proceed in two steps. First, the inclusion evolves under stress-free conditions until its fraction reaches  $f = 0.1$ . Then, a macroscopic mechanical load is applied until failure.

The problem is depicted in Fig. 18. Periodic boundary conditions (PBC) are imposed on the edges ( $\partial V$ ) in order to treat the problem only on a Representative Elementary Volume (REV). PBC are applied by constraining all degrees of freedom to take the same value at two opposite points of  $\partial V$ . During the loading step, a vertical mean strain is imposed by constraining the displacement difference ( $\Delta u$ ) along the  $y$ -direction between two opposite points respectively located on the bottom and top faces. The applied PBC are summarized by:

$$\begin{cases} u_y(x, y = 1, t) - u_y(x, y = 0, t) = \Delta u, \\ u_x(x, y = 1, t) - u_x(x, y = 0, t) = 0, \\ u_x(x = 0, y, t) - u_x(x = 1, y, t) = 0, \\ d(x, y = 1, t) - d(x, y = 0, t) = 0, \\ d(x = 0, y, t) - d(x = 1, y, t) = 0. \end{cases} \quad (52)$$

The mean strain is applied with a relatively high rate compared to the phase transformation kinetics. This avoids a morphological change of the inclusion during the loading step.

A single circular inclusion which an initial radius of  $r_0 = 2 \times 10^{-2}$  is placed in the center of the matrix. Initially, the inclusion is saturated ( $c = c_i$ ) and evolves under the matrix supersaturation ( $c = c_m + 0.5$ ).

The fracture and chemical parameters used for the computation are summarized in Table 3. For sake of brevity, the inclusion and the matrix are supposed to have the same  $g_c$ . The other parameters are specified for each studied case. A regular mesh of  $250 \times 250$  linear quadrangular elements is used and the energy constraint is set to  $\eta = 1\%$ .

Fig. 19 shows the crack topology obtained in the reference case ( $\epsilon^* = 0$ ,  $A_m = A_i = 0$ ) depending on whether the inclusion is stiffer or softer than the matrix. When the inclusion is stiffer than the matrix ( $E_i > E_m$ , Fig. 19(a)), the crack initiation occurs at the poles of the inclusion. Whereas when the inclusion is softer than the matrix ( $E_i < E_m$ , Fig. 19(b)), the crack initiation occurs at the equator of the inclusion. This remains true in the elastic ( $\epsilon^* = 0.05$ ,  $A_m = A_i = 0$ ) and viscoplastic ( $\epsilon^* = 0.05$ ,  $A_m = A_i = 100$ ) cases. The viscoplastic activity and residual stresses induced by the inclusion growth strain have no influence on the crack topology in this example.

However an effect of viscoplasticity and residual stresses is observed when examining  $\langle \sigma_{yy}^c \rangle$  and  $U_I$  as illustrated in Table 4. It can be seen that the values of  $\langle \sigma_{yy}^c \rangle$  and  $U_I$  in the viscoplastic case are always between the reference and the elastic cases. Stress relaxation induced by viscoplastic activity introduces an intermediate fracture behavior between the reference and elastic behavior.

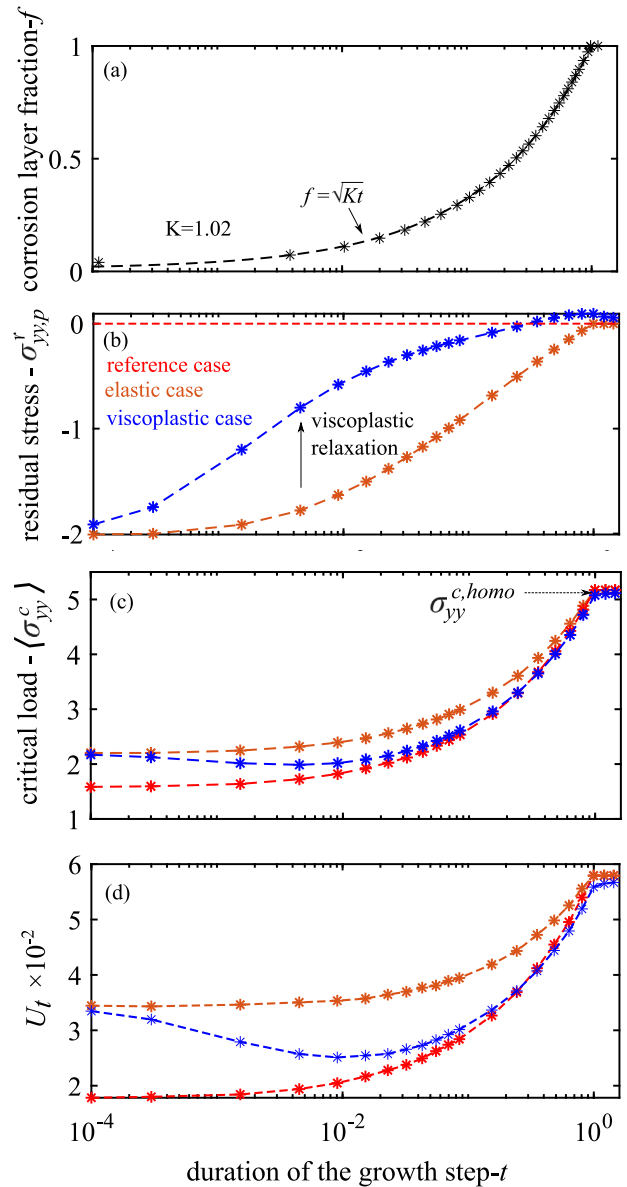


Fig. 16. (a) Parabolic oxide layer growth kinetics. The parabolic constant  $K = 1.02$  corresponds to the best fit of the data by least square methods. (b) The residual stress ( $\sigma_{yy}^r$ ) at the control point after the oxide layer growth step for the reference ( $\epsilon^* = 0$ ,  $A_o = A_m = 0$ ), elastic ( $\epsilon^* = 0.01$ ,  $A_o = A_m = 0$ ) and viscoplastic ( $\epsilon^* = 0.01$ ,  $A_o = A_m = 1$ ) cases. (c) and (d) respectively show the critical load ( $\langle \sigma_{yy}^c \rangle$ ) and  $U_I$  at oxide layer failure.

Table 3

Dimensionless material parameters used for the simulation of the growth of an inclusion. The subscripts  $i, m$  respectively refers to the inclusion ( $\phi = 1$ ) and to the matrix ( $\phi = 0$ ).

Elastic:	$\nu_m = \nu_i$	0.3
Fracture:	$g_m = g_i$	$2 \times 10^{-3}$
	$l_c$	$8 \times 10^{-3}$
Chemical:	$\omega$	$5 \times 10^{-2}$
	$\delta$	0.04
	$M$	$10^6$
	$D_m = D_i = D$	1
	$c_m$	1.33
	$c_i$	1.75
	$k_m = k_i$	100

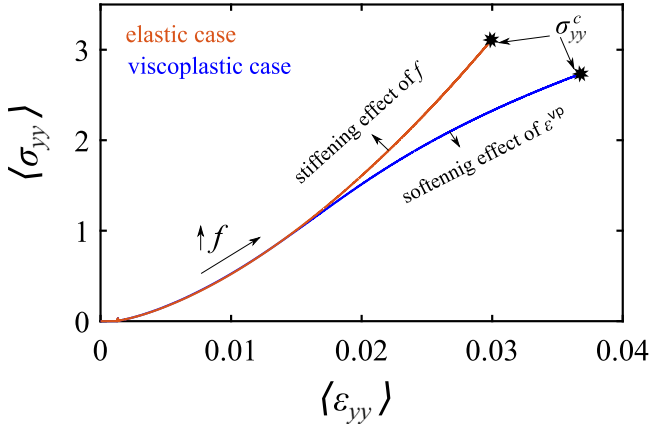


Fig. 17. Effect of low rate monotonic mechanical load during oxide layer growth. Macroscopic stress–strain curve in the elastic case ( $\varepsilon^* = 0.01, A_p = A_m = 0$ ) and viscoplastic case ( $\varepsilon^* = 0.01, A_p = A_m = 0.01$ ).

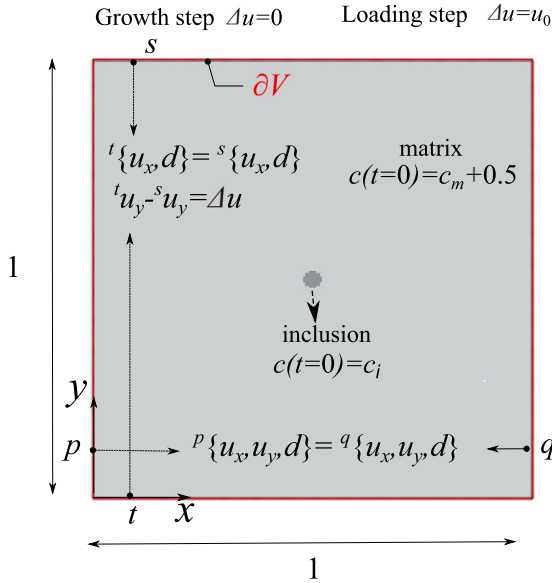


Fig. 18. A unit cell of periodic binary material used to study the fracture topology during the growth of a single inclusion. We proceed in two steps. Firstly, the saturated inclusion ( $c(t = 0) = c_i$ ) grows under matrix supersaturation ( $c(t = 0) = c_m + 0.5$ ) without external applied stress ( $\Delta u = 0$ ) until its fraction reaches  $f = 0.1$ . Secondly, a high rate macroscopic vertical mean strain is applied ( $\Delta u = u_0$ ) until failure.

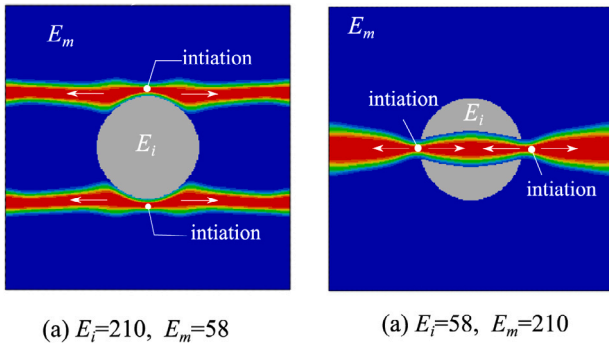


Fig. 19. Fracture topology during the growth of a single inclusion for the reference case ( $\varepsilon^* = 0, A_i = A_m = 0$ ). In (a) the inclusion is stiffer than the matrix. In (b) the inclusion is softer than the matrix. The arrows indicate the propagation direction from crack initiation.

Table 4

Energy density until failure ( $U_i$ ) and critical load ( $\langle \sigma_{yy}^c \rangle$ ) after the growth of a single inclusion for the reference case ( $\varepsilon^* = 0, A_m = A_i = 0$ ), elastic case ( $\varepsilon^* = 0.05, A_m = A_i = 0$ ) and viscoplastic case ( $\varepsilon^* = 0.05, A_m = A_i = 100$ ). In all cases, the growth step is stopped when the inclusion fraction reaches  $f = 0.1$ . Then, the loading is applied until failure.

Rigid inclusion ( $E_i = 210, E_m = 58$ )			
	Reference	Viscoplastic	Elastic
$\langle \sigma_{yy}^c \rangle$ :	3.57	3.64	3.81
$U_i \times 10^{-2}$ :	7.43	7.95	8.85
Soft inclusion ( $E_i = 58, E_m = 210$ )			
	Reference	Viscoplastic	Elastic
$\langle \sigma_{yy}^c \rangle$ :	5.59	5.03	3.25
$U_i \times 10^{-2}$ :	6.47	5.81	2.49

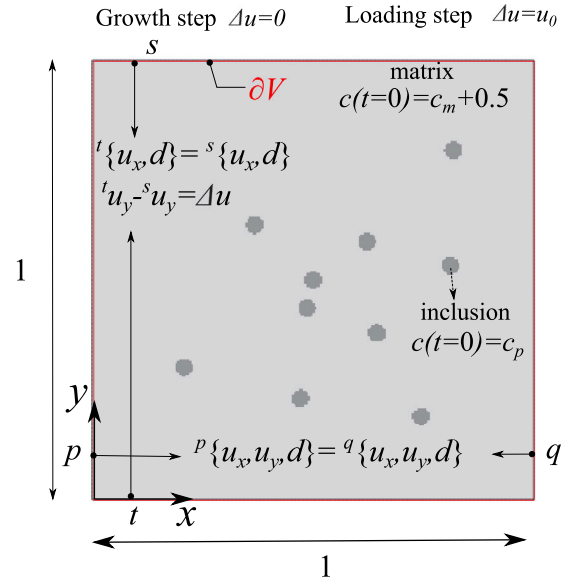


Fig. 20. A unit cell of periodic binary elastic material used to study the crack path induced by a mechanical loading during the Ostwald ripening process. We proceed in two step. Firstly, the saturated inclusions ( $c(t = 0) = c_i$ ) grow under matrix supersaturation ( $c(t = 0) = c_m + 0.5$ ) without external applied stress ( $\Delta u = 0$ ). Secondly, a high rate macroscopic vertical mean strain is applied ( $\Delta u = u_0$ ) until failure.

### 3.4. Heterogeneous case with non planar interface: several inclusions

Here, the model of the previous example is analyzed by considering several initial rigid inclusions that evolve in a soft matrix. This problem, known as the Ostwald ripening phenomenon, is a process that can be observed in heterogeneous solids. During such a process, small inclusions dispersed in a matrix evolve to minimize the total free energy of the system (Alloyeau et al., 2010; Kabalnov, 2001). The evolution takes place mainly by the coalescence of neighboring inclusions or by the growth of large inclusions at the expense of the smallest inclusions as already illustrated by Ammar et al. (2014). The aim of this section is to study the effect of such a process on the crack topology.

A two-step analysis is performed. First, the inclusions evolve under stress-free conditions (Ostwald ripening or growth step). Then, a vertical mean strain is applied until failure (loading step). Fig. 20 gives an illustration of the problem.

Several circular inclusions with an initial radius of  $r_0 = 2 \cdot 10^{-2}$  are randomly distributed in the matrix. Initially, the inclusions are saturated ( $c = c_i$ ) and evolve under the matrix supersaturation ( $c = c_m + 0.5$ ). The material parameters used for the computation are summarized in Table 5. In this example, the chemical properties are chosen so that the internal stress has a significant effect on the growth morphology.

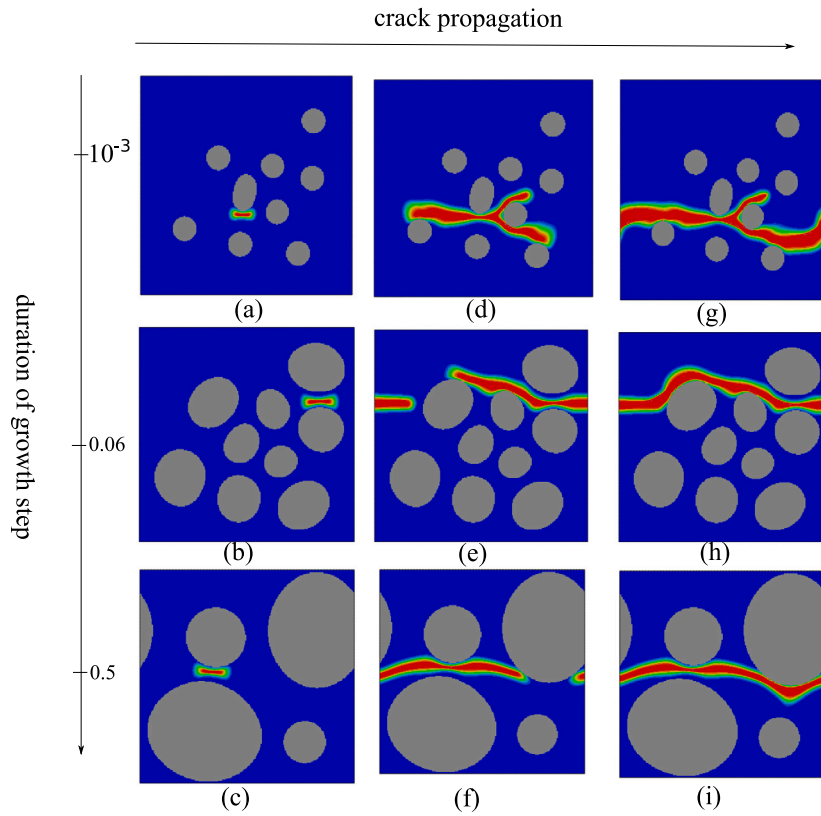


Fig. 21. Crack initiation and propagation through a matrix-inclusion network for different stages of the Ostwald ripening process. (a)–(c) show the initiation while (d)–(i) depict the propagation during the Ostwald ripening process.

Table 5

Dimensionless material parameters used for the simulation of the Ostwald ripening process. The subscripts  $i, m$  respectively refer to the inclusion ( $\phi = 1$ ) and the matrix ( $\phi = 0$ ).

Elasticity:	$E_m$	58
	$E_i$	210
	$\nu_m = \nu_i = \nu$	0.3
Fracture:	$g_m = g_i$	$2 \times 10^{-3}$
	$l_c$	$8 \times 10^{-3}$
Chemical:	$\omega$	$5 \times 10^{-4}$
	$\delta$	0.04
	$M$	$10^6$
	$D_m = D_i$	1
	$c_m$	1.33
	$c_i$	1.75
	$k_m = k_i$	1

Fig. 21 shows the crack topologies obtained at different stages of the Ostwald ripening process in the reference case ( $\epsilon^* = 0, A_i = A_m = 0$ ). It can be seen that cracks always initiate in the matrix between the nearest inclusions aligned in the loading direction (Fig. 21(a)–(c)). The cracks then propagate by bypassing the inclusions encountered along their propagation path (Fig. 21(d)–(i)). When the inclusion encountered is small, a bifurcation is observed (Fig. 21(d) and (g)), but if the inclusion is large, the crack bypasses it without bifurcating (Fig. 21(e), (f), (h) and (i)). From an energy point of view, the observed inclusion bypassing process increases the amount of energy dissipated by the crack compared to the homogeneous case where the crack would propagate in a straight line.

Fig. 22 compares the crack topologies obtained between the reference case ( $\epsilon^* = 0, A_m = A_i = 0$ ), elastic case ( $\epsilon^* = 0.01, A_m = A_i = 0$ ) and viscoplastic case ( $\epsilon^* = 0.01, A_m = A_i = 1$ ) after the same duration of the Ostwald ripening process ( $t = 0.5$ ). A defect ( $d = 1$ ) has been added to the central nodes of the left and right side of the system. The final

morphologies and thus the crack topologies are significantly different in the three cases which shows the importance of taking into account the internal stresses generated during the growth process. Interestingly, we observe that despite the initial defect, cracking can be initiated between two particles when they are very close to each other.

This last example demonstrates the robustness of the proposed multiphase-field model which makes it possible to solve complex shape evolution and crack topology using classical numerical methods.

#### 4. Conclusion

This work presented a multiphase-field model to describe the fracture behavior in viscoplastic non-static binary alloys. For this purpose, the fracture phase-field and phase-field for phase transformation approaches were successfully coupled. Several benchmark examples were shown and results based on the critical loading, energy density until failure and crack topology were discussed.

First, the effect of the loading rate on the fracture behavior of a homogeneous viscoplastic material was studied. At low strain rates ductile fracture response is observed. There was sufficient time for significant energy dissipation by developing viscoplastic deformation, whereas at high strain rates brittle fracture response is observed. The material does not have time to dissipate energy by viscoplastic strain. Plastic activity at the crack tip was found to mitigate the effect of pre-existing defects on mechanical strength.

Second, the effect on the fracture behavior of a rigid oxide layer growing on a soft matrix was also studied. It was shown that the stiffening induced by the growth of an oxide layer improves the macroscopic mechanical strength of the alloy formed. At low strain rates, when viscoplasticity is taken into account, the softening effect induced by viscoplasticity ends up dominating over the stiffening effect of oxide layer growth over time. It was also shown that viscoplasticity

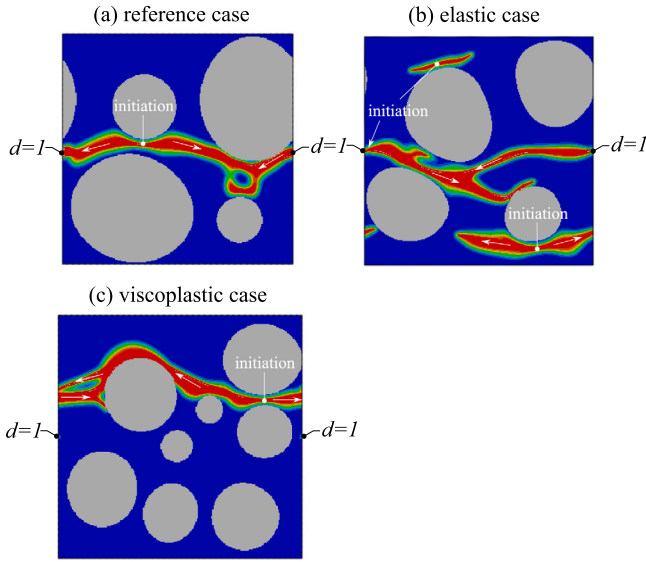


**Fig. 22.** Crack topology after Ostwald ripening process for the reference case ( $\epsilon^* = 0$ ,  $A_m = A_i = 0$ ), elastic case ( $\epsilon^* = 0.01$ ,  $A_m = A_i = 0$ ) and viscoplastic case ( $\epsilon^* = 0.01$ ,  $A_m = A_i = 1$ ). The duration of the growth step was set to  $t = 0.5$ . The loading was applied in vertical direction. The arrows indicate the direction of the crack propagation.

introduces an intermediate fracture behavior between the reference behavior (without residual stresses induced by the phase transformation) and the elastic behavior (with residual stresses taking into account only the elasticity).

The effect of phase morphology and relative stiffness was also studied. With respect to the loading direction, when a particle is more rigid than the matrix, cracking occurs at the poles of the particle. On the other hand, when the particle is less rigid, the initiation occurs at the equator. In case of several rigid inclusions growing in a soft matrix, it has been observed that the area between neighboring inclusions aligned along the loading direction are preferential zones for crack initiation. The crack bypasses the rigid inclusions encountered on its path. Depending on the size of the encountered inclusion, the crack may bifurcate in the case of small inclusions or bypass without bifurcation in the case of large inclusions.

This work presents only simulated results. The question of the experimental validation of the presented model is an important topic that has not been addressed in this paper. In our forthcoming work, this model will be used to simulate the thermomechanical behavior and oxidation of a fuel rod cladding under pressure at high temperature. In this context, improvements of the model taking into account the microstructure of the oxide film may be necessary. Improvements are also needed to better describe the mechanisms associated with ductile fracture and take into account large deformations (Miehe et al., 2016a). Furthermore, in order to simulate the oxidation under stress phenomenon generally observed at low strain rates, the mass transport and probably the phase transformation equation in the damaged region must be adjusted.

## Acknowledgments

The authors thank Antoine Ambard from Electricité de France for the interesting discussions. This work was financially supported by EDF.

## Appendix A. Second law of thermodynamics

Based on the theory of generalized stresses (Gurtin, 1996), we note by  $\{\sigma, \xi, \pi, \omega\}$  the microforce system which are respectively the energetic duals of  $\{\nabla^s \mathbf{u}, \nabla \phi, \phi, d\}$ .  $\sigma$  is the classical Cauchy stress tensor,  $\xi$ ,

$\pi$  are respectively the vector and scalar micro-forces associated with the phase change (Ammar et al., 2009b) and  $\omega$  the driving force associated with fracture (Miehe et al., 2010b). The total internal energy density is the linear combination of the generalized stresses by their respective dual variables:

$$\dot{e} = \pi \dot{\phi} + \xi \cdot \nabla \dot{\phi} + \omega \dot{d} + \sigma : \dot{\epsilon} + g_c \dot{\gamma} \quad (\text{A.1})$$

the last term of the right-hand sides represents the fracture energy density. The local form of the second law of thermodynamics in the isothermal case is given by Ammar et al. (2009b) :

$$T \dot{s} - \nabla \cdot (\mu \mathbf{J}) \geq 0 \quad (\text{A.2})$$

where  $s$  is the entropy density,  $T$  is the temperature,  $\mu$  is the chemical potential and  $\mathbf{J}$  is the chemical flux. The Helmholtz free energy ( $\psi$ ), internal energy ( $e$ ) and entropy ( $s$ ) densities are related by the following Legendre transform :

$$\psi = e - Ts \quad (\text{A.3.1})$$

$$\dot{\psi} = \dot{e} - T \dot{s} \quad \text{in isothermal case} \quad (\text{A.3.2})$$

The local mass conservation equation is given by Ammar et al. (2014):

$$\dot{c} = -\nabla \cdot \mathbf{J} \quad (\text{A.4})$$

Combining Eqs. (A.1) to (A.4) leads to the Clausius–Duhem inequality :

$$-\dot{\psi} + \pi \dot{\phi} + \xi \cdot \nabla \dot{\phi} + \omega \dot{d} + \sigma : \dot{\epsilon} + g_c \dot{\gamma} - \mathbf{J} \cdot \nabla \mu + \mu \dot{c} \geq 0 \quad (\text{A.5})$$

The time derivation of the Helmholtz free energy density is given by :

$$\dot{\psi}(\epsilon^{el}, c, \phi, \nabla \phi, d) = \frac{\partial \psi}{\partial \epsilon^{el}} : \dot{\epsilon}^{el} + \frac{\partial \psi}{\partial c} \dot{c} + \frac{\partial \psi}{\partial \phi} \dot{\phi} + \frac{\partial \psi}{\partial \nabla \phi} \cdot \nabla \dot{\phi} + \frac{\partial \psi}{\partial d} \dot{d} \quad (\text{A.6})$$

Replacing Eq. (A.6) in Eq. (A.5) gives :

$$\begin{aligned} \left( \sigma - \frac{\partial \psi}{\partial \epsilon^{el}} \right) : \dot{\epsilon}^{el} + \left( \mu - \frac{\partial \psi}{\partial c} \right) \dot{c} + \left( \pi - \frac{\partial \psi}{\partial \phi} \right) \dot{\phi} + \left( \xi - \frac{\partial \psi}{\partial \nabla \phi} \right) \cdot \nabla \dot{\phi} \\ + \left( \omega - \frac{\partial \psi}{\partial d} \right) \dot{d} \\ - \mathbf{J} \cdot \nabla \mu + \sigma : \dot{\epsilon}^{vp} + g_c \dot{\gamma} \geq 0 \end{aligned} \quad (\text{A.7})$$

Assuming that the Cauchy tensor ( $\sigma$ ), the chemical potential ( $\mu$ ) and the generalized stress vector ( $\xi$ ) are respectively independent of  $\dot{\epsilon}^{el}$ ,  $\dot{c}$  and  $\nabla \dot{\phi}$  gives the following state laws (de Rancourt et al., 2016):

$$\sigma = \frac{\partial \psi}{\partial \epsilon^{el}} \quad (\text{A.8.1})$$

$$\mu = \frac{\partial \psi}{\partial c} \quad (\text{A.8.2})$$

$$\xi = \frac{\partial \psi}{\partial \nabla \phi} \quad (\text{A.8.3})$$

The dissipation rate inequality is then reduced to :

$$D = \sigma : \dot{\epsilon}^{vp} - \mathbf{J} \cdot \nabla \mu + \pi_{dis} \dot{\phi} + \omega_{dis} \dot{d} + g_c \dot{\gamma} \geq 0 \quad (\text{A.9})$$

where  $\pi_{dis}$  and  $\omega_{dis}$  are defined by :

$$\pi_{dis} = \pi - \frac{\partial \psi}{\partial \phi} \quad (\text{A.10.1})$$

$$\omega_{dis} = \omega - \frac{\partial \psi}{\partial d} \quad (\text{A.10.2})$$

As done in Ammar et al. (2009b), a convex dissipation potential function is defined to ensure the dissipation rate inequality :

$$\begin{aligned} \Omega(\sigma_{vm}, \nabla \mu, \pi_{dis}, \phi) &= h(\phi) \Omega_a(\sigma_{vm}, \nabla \mu, \pi_{dis}) + \bar{h}(\phi) \Omega_b(\sigma_{vm}, \nabla \mu, \pi_{dis}) \\ &= h(\phi) \frac{A_a \sigma_{vm}^{n_a+1}}{n_a+1} + \bar{h}(\phi) \frac{A_b \sigma_{vm}^{n_b+1}}{n_b+1} \\ &+ \frac{1}{2} (L(\phi) \nabla \mu \cdot \nabla \mu + M \pi_{dis}^2) \end{aligned} \quad (\text{A.11})$$

where  $M$  is the interface mobility and  $L(\phi)$  is the homogenized diffusion coefficient (Onsager coefficient). The complementary evolution laws are then derived from the dissipation potential :

$$\dot{\varepsilon}_{vm}^{vp} = \frac{\partial \Omega}{\partial \sigma_{vm}} = h(\phi)A_a \sigma_{vm}^{n_a} + \bar{h}(\phi)A_b \sigma_{vm}^{n_b} \quad (\text{Norton's law}) \quad (\text{A.12.1})$$

$$\dot{\phi} = \frac{\partial \Omega}{\partial \pi_{dis}} = M \pi_{dis} \quad (\text{A.12.2})$$

$$\mathbf{J} = -\frac{\partial \Omega}{\partial \nabla \mu} = -L(\phi) \nabla \mu \quad (\text{Fick's law}) \quad (\text{A.12.3})$$

$$\frac{\partial \Omega}{\partial \omega_{dis}} = 0 \rightarrow \omega = \frac{\partial \psi}{\partial d} \quad (\text{A.12.4})$$

The dissipation rate inequality is then further reduced to :

$$D = \Omega(\sigma_{vm}, \nabla \mu, \pi_{dis}, \phi) + g_c \dot{\gamma} \geq 0 \quad (\text{A.13})$$

This inequality ensures that the second law of thermodynamics is respected.

## Appendix B. Finite element implementation

The strong forms of the four coupled problems (displacement, diffusion, phase transformation, fracture) to be solved are summarized as follows:

$$\begin{cases} \nabla \cdot \boldsymbol{\sigma} - \mathbf{f}_v = 0, \\ \dot{c} + \nabla \cdot \left( L(\phi) \nabla \left( \frac{\partial \psi}{\partial c} \right) \right) = 0, \\ -\alpha \Delta \phi + \frac{\dot{\phi}}{M} + \frac{\partial \psi}{\partial \phi} = 0, \\ \frac{g_c}{l_c} (d - l_c^2 \Delta d) = 2(1-d)\mathcal{H}. \end{cases} \quad (\text{B.1})$$

A Newton–Raphson method is used to solve the multiphysics problem iteratively:

$$\begin{bmatrix} \mathbf{K}_{uu} & \mathbf{K}_{u\phi} & \mathbf{0} & \mathbf{0} \\ \mathbf{K}_{\phi u} & \mathbf{K}_{\phi\phi} & \mathbf{K}_{\phi c} & \mathbf{0} \\ \mathbf{0} & \mathbf{K}_{c\phi} & \mathbf{K}_{cc} & \mathbf{0} \\ \mathbf{0} & \mathbf{0} & \mathbf{0} & \mathbf{K}_{dd} \end{bmatrix} \begin{bmatrix} \mathbf{u}_{n+1} \\ \phi_{n+1} \\ c_{n+1} \\ d_{n+1} \end{bmatrix} = - \begin{bmatrix} \mathbf{r}_n^u \\ \mathbf{r}_n^\phi \\ \mathbf{r}_n^c \\ \mathbf{r}_n^d \end{bmatrix}, \quad (\text{B.2})$$

the corresponding residue vectors read as:

$$\mathbf{r}_i^u = \int_V \left( \mathbf{B}_{ij} \boldsymbol{\sigma}_j - \mathbf{N}_{ij} \mathbf{f}_{vj} \right) dV - \int_{\partial V} \mathbf{N}_{ij} \bar{\mathbf{t}}_j dS, \quad (\text{B.3})$$

$$\mathbf{r}_i^c = \int_V \left\{ \mathbf{N}_i \mathbf{N}_j \dot{c}_j - L(\phi) \mathbf{B}_{ij} \left[ \nabla \left( \frac{\partial \psi}{\partial c} \right) \right]_j \right\} dV + \int_{\partial V} \mathbf{N}_i (\bar{\mathbf{J}} \cdot \mathbf{n}) dS, \quad (\text{B.4})$$

$$\mathbf{r}_i^\phi = \int_V \left\{ \mathbf{N}_i \left( \frac{\dot{\phi}}{M} + \frac{\partial \psi}{\partial \phi} \right) - \alpha \mathbf{B}_{ij} (\nabla \phi)_j \right\} dV, \quad (\text{B.5})$$

$$\mathbf{r}_i^d = \int_V \left\{ \mathbf{N}_i \left( \frac{g_c}{l_c} d - 2(1-d)\mathcal{H} \right) + g_c l_c \mathbf{B}_{ij} (\nabla d)_j \right\} dV. \quad (\text{B.6})$$

In Eq. (B.4),  $\bar{\mathbf{J}}$  is the external chemical flux. The matrix of shape functions and its derivatives used for the discretization of the scalar quantities  $\mathbf{N}$ ,  $\mathbf{B}$  and the vector quantities  $\underline{\mathbf{N}}$ ,  $\underline{\mathbf{B}}$  are given by:

$$\mathbf{N} = [N_1 \quad N_2 \quad \dots \quad N_n] \quad (\text{B.7})$$

$$\underline{\mathbf{N}} = \begin{bmatrix} N_1 & 0 & N_2 & 0 & \dots & N_n & 0 \\ 0 & N_1 & 0 & N_2 & \dots & 0 & N_n \end{bmatrix} \quad (\text{B.8})$$

$$\mathbf{B} = \begin{bmatrix} \frac{\partial N_1}{\partial x} & \frac{\partial N_2}{\partial x} & \dots & \frac{\partial N_n}{\partial x} \\ \frac{\partial N_1}{\partial y} & \frac{\partial N_2}{\partial y} & \dots & \frac{\partial N_n}{\partial y} \end{bmatrix} \quad (\text{B.9})$$

$$\underline{\mathbf{B}} = \begin{bmatrix} \frac{\partial N_1}{\partial x} & 0 & \frac{\partial N_2}{\partial x} & 0 & \dots & \frac{\partial N_n}{\partial x} & 0 \\ 0 & \frac{\partial N_1}{\partial y} & 0 & \frac{\partial N_2}{\partial y} & \dots & 0 & \frac{\partial N_n}{\partial y} \\ \frac{\partial N_1}{\partial y} & \frac{\partial N_1}{\partial x} & \frac{\partial N_2}{\partial y} & \frac{\partial N_2}{\partial x} & \dots & \frac{\partial N_n}{\partial y} & \frac{\partial N_n}{\partial x} \end{bmatrix} \quad (\text{B.10})$$

In Eq. (B.2) the tangents matrices are calculated as follows:

$$[\mathbf{K}_{uu}]_{ij} = \int_V \left\{ \mathbf{B}_{ik}^T \left( \frac{\partial^2 \psi^{el}}{\partial \boldsymbol{\varepsilon}^2} \right)_{kl} \mathbf{B}_{lj} \right\} dV \quad (\text{B.11})$$

$$[\mathbf{K}_{u\phi}]_{ij} = \int_V \left\{ \mathbf{B}_{ik}^T \left( \frac{\partial^2 \psi^{el}}{\partial \phi \partial \boldsymbol{\varepsilon}} \right)_k \mathbf{N}_j \right\} dV \quad (\text{B.12})$$

$$[\mathbf{K}_{\phi u}]_{ij} = - \int_V \left\{ \mathbf{N}_i \left( \frac{\partial^2 \psi}{\partial \boldsymbol{\varepsilon} \partial \phi} \right)_k \mathbf{B}_{kj} \right\} dV \quad (\text{B.13})$$

$$[\mathbf{K}_{\phi c}]_{ij} = - \int_V \left\{ \frac{\partial^2 \psi}{\partial c \partial \phi} \mathbf{N}_i \mathbf{N}_j \right\} dV \quad (\text{B.14})$$

$$[\mathbf{K}_{\phi\phi}]_{ij} = - \int_V \left\{ \left( \frac{1}{M \Delta t} + \frac{\partial^2 \psi}{\partial \phi^2} \right) \mathbf{N}_i \mathbf{N}_j + \alpha \mathbf{B}_{ik}^T \mathbf{B}_{kj} \right\} dV \quad (\text{B.15})$$

$$[\mathbf{K}_{dd}]_{ij} = \int_V \left\{ \mathbf{N}_i \mathbf{N}_j \left( \frac{g_c}{l_c} + 2\mathcal{H} \right) + g_c l_c \mathbf{B}_{ik}^T \mathbf{B}_{kj} \right\} dV \quad (\text{B.16})$$

$$[\mathbf{K}_{cc}]_{ij} = \int_V \left\{ \frac{1}{\Delta t} \mathbf{N}_i \mathbf{N}_j + L(\phi) \mathbf{B}_{ik}^T \left[ \left( \frac{\partial^3 \psi}{\partial c^3} \right) (\nabla c)_k \mathbf{N}_j + \left( \frac{\partial^3 \psi}{\partial c \partial \phi \partial c} \right) (\nabla \phi)_k \mathbf{N}_j + \frac{\partial^2 \psi}{\partial c^2} \mathbf{B}_{kj} \right] \right\} dV \quad (\text{B.17})$$

Note that the global stiffness matrix is not symmetric. The problem is solved with a non symmetric solver.

## Appendix C. Useful derivatives for implementation

### C.1. Helmholtz free energy density derivatives

The derivatives of the Helmholtz free energy density ( $\psi$ ) required for the calculation of the residuals and stiffness matrix are given below:

$$\frac{\partial \psi}{\partial \boldsymbol{\varepsilon}^{el} \partial \phi} = \mathbb{C} : \frac{\partial \boldsymbol{\varepsilon}^{el}}{\partial \phi} + h'(\phi) (\mathbb{C}_a - \mathbb{C}_b) : \boldsymbol{\varepsilon}^{el}, \quad (\text{C.1})$$

$$\begin{aligned} \frac{\partial \psi}{\partial \phi} &= \frac{\partial \psi^{el}}{\partial \phi} + \frac{\partial \psi^{ch}}{\partial \phi} \\ &= \frac{\partial \boldsymbol{\varepsilon}^{el}}{\partial \phi} : \mathbb{C} : \boldsymbol{\varepsilon}^{el} + \frac{h'(\phi)}{2} \boldsymbol{\varepsilon}^{el} : (\mathbb{C}_a - \mathbb{C}_b) \\ &\quad : \boldsymbol{\varepsilon}^{el} + W g'(\phi) + h'(\phi) (\psi_a^{ch} - \psi_b^{ch}), \end{aligned} \quad (\text{C.2})$$

$$\begin{aligned} \frac{\partial^2 \psi}{\partial \phi^2} &= \frac{\partial^2 \psi^{el}}{\partial \phi^2} + \frac{\partial^2 \psi^{ch}}{\partial \phi^2} \\ &= \frac{\partial^2 \boldsymbol{\varepsilon}^{el}}{\partial \phi^2} : \mathbb{C} : \boldsymbol{\varepsilon}^{el} + 2h'(\phi) \frac{\partial \boldsymbol{\varepsilon}^{el}}{\partial \phi} : (\mathbb{C}_a - \mathbb{C}_b) : \boldsymbol{\varepsilon}^{el} \\ &\quad + \frac{\partial \boldsymbol{\varepsilon}^{el}}{\partial \phi} : \mathbb{C} : \frac{\partial \boldsymbol{\varepsilon}^{el}}{\partial \phi} + \frac{h''(\phi)}{2} \boldsymbol{\varepsilon}^{el} : (\mathbb{C}_a - \mathbb{C}_b) \\ &\quad : \boldsymbol{\varepsilon}^{el} + W g''(\phi) + h''(\phi) (\psi_a^{ch} - \psi_b^{ch}), \end{aligned} \quad (\text{C.3})$$

$$\frac{\partial^2 \psi}{\partial c \partial \phi} = h'(\phi) k_a (c - c_a) - h'(\phi) k_b (c - c_b), \quad (\text{C.4})$$

$$\frac{\partial^3 \psi}{\partial c \partial \phi^2} = h''(\phi) k_a (c - c_a) - h''(\phi) k_b (c - c_b), \quad (\text{C.5})$$

$$\frac{\partial^3 \psi}{\partial c^2 \partial \phi} = h'(\phi) (k_a - k_b), \quad (\text{C.6})$$

where  $\mathbb{C}$  is the stiffness matrix.

## C.2. Elastic strain energy derivatives

The derivatives of the elastic strain ( $\epsilon^{el}$ ), required for the calculation of the derivatives of the Helmholtz free energy are given below:

$$\frac{\partial \epsilon^{el}}{\partial \phi} = h'(\phi) (\epsilon_b^* + \epsilon_b^{vp} - \epsilon_a^* - \epsilon_a^{vp}) \quad (C.7)$$

$$\frac{\partial^2 \epsilon^{el}}{\partial \phi^2} = h''(\phi) (\epsilon_b^* + \epsilon_b^{vp} - \epsilon_a^* - \epsilon_a^{vp}) \quad (C.8)$$

## References

- Allen, S.M., Cahn, J.W., 1979. A microscopic theory for antiphase boundary motion and its application to antiphase domain coarsening. *J. Appl. Phys.* 50, 1085–1095. [http://dx.doi.org/10.1016/0001-6160\(79\)90196-2](http://dx.doi.org/10.1016/0001-6160(79)90196-2). URL: <http://www.sciencedirect.com/science/article/pii/0001616079901962>.
- Alloyeau, D., Prévot, G., Le Bouar, Y., Oikawa, T., Langlois, C., Loiseau, A., Ricolleau, C., 2010. Ostwald ripening in nanoalloys: When thermodynamics drives a size-dependent particle composition. *Phys. Rev. Lett.* 105 (25), 255901. <http://dx.doi.org/10.1103/PhysRevLett.105.255901>, URL: <https://link.aps.org/doi/10.1103/PhysRevLett.105.255901>. Publisher: American Physical Society.
- Ambati, M., Gerasimov, T., De Lorenzis, L., 2015a. Phase-field modeling of ductile fracture. *Comput. Mech.* 55 (5), 1017–1040. <http://dx.doi.org/10.1007/s00466-015-1151-4>.
- Ambati, M., Gerasimov, T., De Lorenzis, L., 2015b. A review on phase-field models of brittle fracture and a new fast hybrid formulation. *Comput. Mech.* 55 (2), 383–405. <http://dx.doi.org/10.1007/s00466-014-1109-y>.
- Ammar, K., Appolaire, B., Caillaud, G., Forest, S., 2009a. Combining phase field approach and homogenization methods for modelling phase transformation in elastoplastic media. *Eur. J. Comput. Mech.* 18 (5–6), 485–523. <http://dx.doi.org/10.3166/ejcm.18.485-523>, arXiv:<https://doi.org/10.3166/ejcm.18.485-523>.
- Ammar, K., Appolaire, B., Caillaud, G., Forest, S., 2009b. Combining phase field approach and homogenization methods for modelling phase transformation in elastoplastic media. *Eur. J. Comput. Mech.* 18 (5–6), 485–523. <http://dx.doi.org/10.3166/ejcm.18.485-523>, Publisher: Taylor & Francis. eprint: <https://doi.org/10.3166/ejcm.18.485-523>.
- Ammar, K., Appolaire, B., Forest, S., Cottura, M., Bouar, Y.L., Finel, A., 2014. Modelling inheritance of plastic deformation during migration of phase boundaries using a phase field method. *J. Mech. Phys. Solids* 67, 2699–2717. <http://dx.doi.org/10.1016/j.jmps.2014.09.005>, URL: <https://www.sciencedirect.com/science/article/pii/S0022509615303938>.
- Asle Zaem, M., Yin, H., Felicelli, S.D., 2013. Modeling dendritic solidification of Al–3%Cu using cellular automaton and phase-field methods. *Appl. Math. Model.* 37 (5), 3495–3503. <http://dx.doi.org/10.1016/j.apm.2012.08.005>, URL: <http://www.sciencedirect.com/science/article/pii/S0307904X12004611>.
- Badnava, H., Etemadi, E., Msekh, M.A., 2017. A phase field model for rate-dependent ductile fracture. *Metals* 7 (5), <http://dx.doi.org/10.3390/met7050180>, URL: <https://www.mdpi.com/2075-4701/7/5/180>. Number: 5 keywords=ductile fracture, finite element, phase field, rate dependency, viscoplasticity, pages=180.
- Bazant, Z.P., 1984. Size effect in blunt fracture: Concrete, rock, metal. *J. Eng. Mech.* 110 (4), 518–535. [http://dx.doi.org/10.1061/\(ASCE\)0733-9399\(1984\)110:4\(518\)](http://dx.doi.org/10.1061/(ASCE)0733-9399(1984)110:4(518)), URL: <https://ascelibrary.org/doi/abs/10.1061/%28ASCE%290733-9399%281984%29110%3A4%28518%29>. Publisher: American Society of Civil Engineers.
- Bernard, P.E., Moës, N., Chevaugeon, N., 2012. Damage growth modeling using the thick level set (TLS) approach: Efficient discretization for quasi-static loadings. *Comput. Methods Appl. Mech. Engrg.* 233–236, 11–27. <http://dx.doi.org/10.1016/j.cma.2012.02.020>, URL: <http://www.sciencedirect.com/science/article/pii/S004578251200062X>.
- Bhattacharya, A., Mondal, K., Upadhyay, C.S., Sangal, S., 2020. A phase-field investigation of the effect of grain-boundary diffusion on austenite to ferrite transformation. *Comput. Mater. Sci.* 173, 109428. <http://dx.doi.org/10.1016/j.commatsci.2019.109428>, URL: <https://www.sciencedirect.com/science/article/pii/S092702561930727X>.
- Bourdin, B., Francfort, G.A., Marigo, J.-J., 2000. Numerical experiments in revisited brittle fracture. *J. Mech. Phys. Solids* 48 (4), 797–826. [http://dx.doi.org/10.1016/S0022-5096\(99\)00028-9](http://dx.doi.org/10.1016/S0022-5096(99)00028-9), URL: <https://www.sciencedirect.com/science/article/pii/S0022509699000289>.
- Campello, D., Tardif, N., Mouta, M., Baietto, M.C., Coret, M., Desquines, J., 2017. Identification of the steady-state creep behavior of zirconium claddings under simulated loss-of-coolant accident conditions based on a coupled experimental/numerical approach. *Int. J. Solids Struct.* 115–116, 190–199. <http://dx.doi.org/10.1016/j.ijsolstr.2017.03.016>, URL: <http://www.sciencedirect.com/science/article/pii/S002076831730121X>.
- Carrara, P., Ambati, M., Alessi, R., De Lorenzis, L., 2020. A framework to model the fatigue behavior of brittle materials based on a variational phase-field approach. *Comput. Methods Appl. Mech. Engrg.* 361, 112731. <http://dx.doi.org/10.1016/j.cma.2019.112731>, URL: <https://www.sciencedirect.com/science/article/pii/S0045782519306218>.
- Chosson, R., Gourgues-Lorenzon, A., Vandenberghe, V., Brachet, J., Crépin, J., 2016. Creep flow and fracture behavior of the oxygen-enriched alpha phase in zirconium alloys. *Scr. Mater.* 117, 20–23. <http://dx.doi.org/10.1016/j.scriptamat.2016.02.021>, URL: <http://www.sciencedirect.com/science/article/pii/S1359646216300653>.
- Cottura, M., Le Bouar, Y., Finel, A., Appolaire, B., Ammar, K., Forest, S., 2012. A phase field model incorporating strain gradient viscoplasticity: Application to rafting in Ni-base superalloys. *J. Mech. Phys. Solids* 60 (7), 1243–1256. <http://dx.doi.org/10.1016/j.jmps.2012.04.003>, URL: <http://www.sciencedirect.com/science/article/pii/S0022509612000750>.
- de Rancourt, V., Ammar, K., Appolaire, B., Forest, S., 2016. Homogenization of viscoplastic constitutive laws within a phase field approach. *J. Mech. Phys. Solids* 88, 291–319. <http://dx.doi.org/10.1016/j.jmps.2015.12.026>, URL: <http://www.sciencedirect.com/science/article/pii/S0022509615303938>.
- Desquines, J., Duriez, C., Guilbert, S., Taurines, T., 2021. High temperature oxidation and room temperature axial strength of pre-oxidized zirconium-4 cladding after a simulated LOCA. *J. Nucl. Mater.* 543, 152559. <http://dx.doi.org/10.1016/j.jnucmat.2020.152559>, URL: <http://www.sciencedirect.com/science/article/pii/S0022311520311673>.
- Dominguez, C., 2018. Effect of pre-oxide and hydrogen on creep of zirconium-4 at 1123K. *J. Nucl. Mater.* 511, 446–458. <http://dx.doi.org/10.1016/j.jnucmat.2018.09.047>.
- Dreyer, W., Müller, W., 2000. A study of the coarsening in tin/lead solders. *Int. J. Solids Struct.* 37 (28), 3841–3871. [http://dx.doi.org/10.1016/S0020-7683\(99\)00146-8](http://dx.doi.org/10.1016/S0020-7683(99)00146-8), URL: <http://www.sciencedirect.com/science/article/pii/S0020768399001468>.
- Duda, F.P., Ciaronetti, A., Sánchez, P.J., Huespe, A.E., 2015. A phase-field/gradient damage model for brittle fracture in elastic–plastic solids. *Int. J. Plast.* 65, 269–296. <http://dx.doi.org/10.1016/j.ijplas.2014.10.005>, URL: <https://www.sciencedirect.com/science/article/pii/S0749641914001892>.
- Durga, A., Wollants, P., Moelans, N., 2013. Evaluation of interfacial excess contributions in different phase-field models for elastically inhomogeneous systems. *Modelling Simulation Mater. Sci. Eng.* 21 (5), 055018. <http://dx.doi.org/10.1088/0965-0393/21/5/055018>, Publisher: IOP Publishing.
- Düsing, M., Mahnen, R., 2019. A coupled phase field/diffusional/mechanical framework for simulation of upper and lower bainitic transformation. *Int. J. Solids Struct.* 162, 45–59. <http://dx.doi.org/10.1016/j.ijsolstr.2018.11.027>, URL: <http://www.sciencedirect.com/science/article/pii/S0020768318304815>.
- Echebarria, B., Folch, R., Karma, A., Plapp, M., 2004. Quantitative phase-field model of alloy solidification. *Phys. Rev. E* 70, 061604. <http://dx.doi.org/10.1103/PhysRevE.70.061604>, URL: <https://link.aps.org/doi/10.1103/PhysRevE.70.061604>.
- Elguedj, T., Gravouil, A., Combescure, A., 2006. Appropriate extended functions for X-FEM simulation of plastic fracture mechanics. *Comput. Methods Appl. Mech. Engrg.* 195 (7), 501–515. <http://dx.doi.org/10.1016/j.cma.2005.02.007>, URL: <https://www.sciencedirect.com/science/article/pii/S0045782505000976>.
- Falk, M.L., Needleman, A., Rice, J.R., 2001. A critical evaluation of cohesive zone models of dynamic fracture. *J. Phys. IV* 11 (PR5), Pr5–Pr5–50. <http://dx.doi.org/10.1051/jp4:2001506>, Publisher: EDP Sciences.
- Fang, J., Wu, C., Rabczuk, T., Wu, C., Ma, C., Sun, G., Li, Q., 2019. Phase field fracture in elasto-plastic solids: Abaqus implementation and case studies. *Theor. Appl. Fract. Mech.* 103, 102252. <http://dx.doi.org/10.1016/j.tafmec.2019.102252>, URL: <https://www.sciencedirect.com/science/article/pii/S0167844218306141>.
- Godlewski, J., Bouvier, P., Lucazeau, G., Fayette, L., 2000. Stress distribution measured by Raman spectroscopy in zirconia films formed by oxidation of zirconium alloys. In: Sabol, G., Moan, G. (Eds.), *Zirconium in the Nuclear Industry: Twelfth International Symposium*. ASTM International, West Conshohocken, PA, pp. 877–900. <http://dx.doi.org/10.1520/STP14332S>, URL: [https://www.astm.org/DIGITAL\\_LIBRARY/STP/PAGES/STP14332S.htm](https://www.astm.org/DIGITAL_LIBRARY/STP/PAGES/STP14332S.htm).
- Gravouil, A., Pierres, E., Baietto, M.C., 2011. Stabilized global–local X-FEM for 3D non-planar frictional crack using relevant meshes. *Internat. J. Numer. Methods Engrg.* 88 (13), 1449–1475. <http://dx.doi.org/10.1002/nme.3232>, URL: <https://onlinelibrary.wiley.com/doi/abs/10.1002/nme.3232>. eprint: <https://onlinelibrary.wiley.com/doi/pdf/10.1002/nme.3232>.
- Griffith, 1921. The phenomena of rupture and flow in solids. *Philos. Trans. R. Soc. Lond. Ser. A* 221 (582–593), 163–198. <http://dx.doi.org/10.1098/rsta.1921.0006>, URL: <https://royalsocietypublishing.org/doi/abs/10.1098/rsta.1921.0006>. Publisher: Royal Society.
- Griffith, A.A., 1924. The theory of rupture. *First Int. Cong. Appl. Mech.* 55–63.
- Gurtin, M.E., 1996. Generalized Ginzburg–Landau and Cahn–Hilliard equations based on a microforce balance. *Physica D* 92 (3), 178–192. [http://dx.doi.org/10.1016/0167-2789\(95\)00173-5](http://dx.doi.org/10.1016/0167-2789(95)00173-5), URL: <http://www.sciencedirect.com/science/article/pii/0167278995001735>.
- Huespe, A.E., Oliver, J., Sanchez, P.J., Blanco, S., Sonzogni, V., 2006. Strong discontinuity approach in dynamic fracture simulations. p. 22.
- Kabalnov, A., 2001. Ostwald ripening and related phenomena. *J. Dispers. Sci. Technol.* 22 (1), 1–12. <http://dx.doi.org/10.1081/DIS-100102675>, Publisher: Taylor & Francis. eprint: <https://doi.org/10.1081/DIS-100102675>.
- Khachatryan, A.G., Shatalov, G.A., 1969. Theory of macroscopic periodicity of a phase transition in the solid state. *J. Appl. Phys.* 40, 29, 5.
- Kim, S.G., Kim, W.T., Suzuki, T., 1998. Interfacial compositions of solid and liquid in a phase-field model with finite interface thickness for isothermal solidification in binary alloys. *Phys. Rev. E* 58, 3316–3323. <http://dx.doi.org/10.1103/PhysRevE.58.3316>, URL: <https://link.aps.org/doi/10.1103/PhysRevE.58.3316>.

- Labergère, C., Long, M., Badreddine, H., Niane, N.-T., Grange, D., Saanouni, K., 2021. Thermomechanical model for solidification and cooling simulation of Ni-based superalloy components. *Int. J. Solids Struct.* 212, 202–219. <http://dx.doi.org/10.1016/j.ijsolstr.2020.12.009>, URL: <https://www.sciencedirect.com/science/article/pii/S0020768320304844>.
- Le Claire, A.D., Rabinovitch, A., 1981. A mathematical analysis of diffusion in dislocations. I. Application to concentration 'tails'. *J. Phys. Condens. Matter* 14 (27), 3863–3879. <http://dx.doi.org/10.1088/0022-3719/14/27/011>, URL: <http://www.scopus.com/inward/record.url?scp=0000323852&partnerID=8YFLogxK>.
- Le Claire, A.D., Rabinovitch, A., 1982. A mathematical analysis of diffusion in dislocations. II. Influence at low densities on measured diffusion coefficients. *J. Phys. Condens. Matter* 15 (16), 3455–3471. <http://dx.doi.org/10.1088/0022-3719/15/16/007>, URL: <http://www.scopus.com/inward/record.url?scp=3843143703&partnerID=8YFLogxK>.
- Le Claire, A.D., Rabinovitch, A., 1983. A mathematical analysis of diffusion in dislocations. III. Diffusion in a dislocation array with diffusion zone overlap. *J. Phys. Condens. Matter* 16 (11), 2087–2104. <http://dx.doi.org/10.1088/0022-3719/16/11/012>, URL: <http://www.scopus.com/inward/record.url?scp=34047155045&partnerID=8YFLogxK>.
- Le Saux, M., Guilbert, T., Brachet, J.C., 2018. An approach to study oxidation-induced stresses in Zr alloys oxidized at high temperature. *Corros. Sci.* 140, 79–91. <http://dx.doi.org/10.1016/j.corsci.2018.06.016>, URL: <http://www.sciencedirect.com/science/article/pii/S0010938X18306140>.
- Lo, Y.-S., Borden, M.J., Ravi-Chandar, K., Landis, C.M., 2019. A phase-field model for fatigue crack growth. *J. Mech. Phys. Solids* 132, 103684. <http://dx.doi.org/10.1016/j.jmps.2019.103684>, URL: <https://www.sciencedirect.com/science/article/pii/S0022509619306568>.
- Ly, A., Ambard, A., Blat-Yrieix, M., Legras, L., Frankel, P., Preuss, M., Curfs, C., Parry, G., Bréchet, Y., 2011. Understanding crack formation at the metal/oxide interface during corrosion of zircaloy-4 using a simple mechanical model. *J. ASTM Int.* 84, 682–707.
- Mandal, T.K., Nguyen, V.P., Wu, J.-Y., 2020. A length scale insensitive anisotropic phase field fracture model for hyperelastic composites. *Int. J. Mech. Sci.* 188, 105941. <http://dx.doi.org/10.1016/j.iijmecsci.2020.105941>, URL: <http://www.sciencedirect.com/science/article/pii/S0020740320316763>.
- Mesgarnejad, A., Imanian, A., Karma, A., 2019. Phase-field models for fatigue crack growth. *Theor. Appl. Fract. Mech.* 103, 102282. <http://dx.doi.org/10.1016/j.tafmec.2019.102282>, URL: <https://www.sciencedirect.com/science/article/pii/S0167844218306712>.
- Miehe, C., Aldakheel, F., Raina, A., 2016a. Phase field modeling of ductile fracture at finite strains: A variational gradient-extended plasticity-damage theory. *Int. J. Plast.* 84, 1–32. <http://dx.doi.org/10.1016/j.iijplas.2016.04.011>, URL: <https://www.sciencedirect.com/science/article/pii/S0749641916300602>.
- Miehe, C., Dal, H., Schänzel, L., Raina, A., 2016b. A phase-field model for chemo-mechanical induced fracture in lithium-ion battery electrode particles. *Numer. Methods Eng.* 106, 683–711.
- Miehe, C., Hofacker, M., Welschinger, F., 2010a. A phase field model for rate-independent crack propagation: Robust algorithmic implementation based on operator splits. *Comput. Methods Appl. Mech. Engrg.* 199 (45), 2765–2778. <http://dx.doi.org/10.1016/j.cma.2010.04.011>, URL: <http://www.sciencedirect.com/science/article/pii/S0045782510001283>.
- Miehe, C., Welschinger, F., Hofacker, M., 2010b. Thermodynamically consistent phase-field models of fracture: Variational principles and multi-field FE implementations. *Comput. Methods Appl. Mech. Engrg.* 83 (10), 1273–1311. <http://dx.doi.org/10.1002/nme.2861>.
- Moelans, N., Blanpain, B., Wollants, P., 2008. Quantitative analysis of grain boundary properties in a generalized phase field model for grain growth in anisotropic systems. *Phys. Rev. B* 78 (2), 024113. <http://dx.doi.org/10.1103/PhysRevB.78.024113>, URL: <https://link.aps.org/doi/10.1103/PhysRevB.78.024113>. Publisher: American Physical Society.
- Moës, N., Dolbow, J., Belytschko, T., 1999. A finite element method for crack growth without remeshing. *Numer. Methods Eng.* 49, 131–150.
- Moës, N., Stolz, C., Bernard, P.-E., Chevaugeon, N., 2011. A level set based model for damage growth: The thick level set approach. *Internat. J. Numer. Methods Engrg.* 86 (3), 358–380. <http://dx.doi.org/10.1002/nme.3069>, URL: <https://onlinelibrary.wiley.com/doi/abs/10.1002/nme.3069>. eprint: <https://onlinelibrary.wiley.com/doi/pdf/10.1002/nme.3069>.
- Molnár, G., Doitrand, A., Estevez, R., Gravouil, A., 2020a. Toughness or strength? Regularization in phase-field fracture explained by the coupled criterion. *Theor. Appl. Fract. Mech.* 109, 102736. <http://dx.doi.org/10.1016/j.tafmec.2020.102736>, URL: <http://www.sciencedirect.com/science/article/pii/S0167844220303128>.
- Molnár, G., Gravouil, A., 2017. 2D and 3D abaqus implementation of a robust staggered phase-field solution for modeling brittle fracture. *Finite Elem. Anal. Des.* 130, 27–38. <http://dx.doi.org/10.1016/j.finel.2017.03.002>, URL: <http://www.sciencedirect.com/science/article/pii/S0168874X16304954>.
- Molnár, G., Gravouil, A., Seghir, R., Réthoré, J., 2020b. An open-source Abaqus implementation of the phase-field method to study the effect of plasticity on the instantaneous fracture toughness in dynamic crack propagation. *Comput. Methods Appl. Mech. Engrg.* 365, 113004. <http://dx.doi.org/10.1016/j.cma.2020.113004>, URL: <http://www.sciencedirect.com/science/article/pii/S0045782520301882>.
- Mosler, J., Shchyglo, O., Montazer Hojjat, H., 2014. A novel homogenization method for phase field approaches based on partial rank-one relaxation. *J. Mech. Phys. Solids* 68, 251–266. <http://dx.doi.org/10.1016/j.jmps.2014.04.002>, URL: <https://www.sciencedirect.com/science/article/pii/S0022509614000623>.
- Nguyen, T.-T., Bolivar, J., Réthoré, J., Baietto, M.-C., Fregonesi, M., 2017. A phase field method for modeling stress corrosion crack propagation in a nickel base alloy. *Int. J. Solids Struct.* 112, 65–82. <http://dx.doi.org/10.1016/j.ijsolstr.2017.02.019>, URL: <https://www.sciencedirect.com/science/article/pii/S0020768317300744>.
- Nguyen, T.-T., Bolivar, J., Shi, Y., Réthoré, J., King, A., Fregonesi, M., Adrien, J., Buffiere, J.-Y., Baietto, M.-C., 2018. A phase field method for modeling anodic dissolution induced stress corrosion crack propagation. *Corros. Sci.* 132, 146–160. <http://dx.doi.org/10.1016/j.corsci.2017.12.027>, URL: <https://www.sciencedirect.com/science/article/pii/S0010938X17305875>.
- Panicaud, B., Grosseau-Poussard, J.L., Dinhut, J.F., 2006. On the growth strain origin and stress evolution prediction during oxidation of metals. *Appl. Surf. Sci.* 252 (16), 5700–5713. <http://dx.doi.org/10.1016/j.apsusc.2005.07.075>, URL: <https://www.sciencedirect.com/science/article/pii/S0169433205011062>.
- Peng, F., Huang, W., Zhang, Z.-Q., Fu Guo, T., Ma, Y., 2020. Phase field simulation for fracture behavior of hyperelastic material at large deformation based on edge-based smoothed finite element method. *Eng. Fract. Mech.* 238, 107233. <http://dx.doi.org/10.1016/j.engfracmech.2020.107233>, URL: <http://www.sciencedirect.com/science/article/pii/S001379442030816X>.
- Raabe, D., Roters, F., Barlat, F., Chen, L., 2004. Continuum Scale Simulation of Engineering Materials: Fundamentals Microstructures Process Applications. Wesley-VCH, pp. 37–56.
- Réthoré, J., Gravouil, A., Combescure, A., 2005. An energy-conserving scheme for dynamic crack growth using the extended finite element method. *Internat. J. Numer. Methods Engrg.* 63 (5), 631–659. <http://dx.doi.org/10.1002/nme.1283>, URL: <https://onlinelibrary.wiley.com/doi/abs/10.1002/nme.1283>. eprint: <https://onlinelibrary.wiley.com/doi/pdf/10.1002/nme.1283>.
- Reuss, A., Angew, Z., 1929. *Math. Mech.* 9, 49.
- Schneider, D., Schoof, E., Huang, Y., Selzer, M., Nestler, B., 2016. Phase-field modeling of crack propagation in multiphase systems. *Comput. Methods Appl. Mech. Engrg.* 312, 186–195. <http://dx.doi.org/10.1016/j.cma.2016.04.009>, URL: <http://www.sciencedirect.com/science/article/pii/S0045782516301669>. Phase Field Approaches to Fracture.
- Schneider, D., Selzer, M., Bette, J., Rementeria, I., Vondrous, A., Hoffmann, M.J., Nestler, B., 2014. Phase-field modeling of diffusion coupled crack propagation processes. *Adv. Energy Mater.* 16 (2), 142–146. <http://dx.doi.org/10.1002/adem.201300073>, URL: <https://onlinelibrary.wiley.com/doi/abs/10.1002/adem.201300073>. eprint: <https://onlinelibrary.wiley.com/doi/pdf/10.1002/adem.201300073>.
- Shanthraj, P., Sharma, L., Svendsen, B., Roters, F., Raabe, D., 2016. A phase field model for damage in elasto-viscoplastic materials. *Comput. Methods Appl. Mech. Engrg.* 312, 167–185. <http://dx.doi.org/10.1016/j.cma.2016.05.006>, URL: <https://www.sciencedirect.com/science/article/pii/S0045782516303267>.
- Sieradzki, K., Newman, R.C., 1987. Stress-corrosion cracking. *J. Phys. Chem. Solids* 48 (11), 1101–1113. [http://dx.doi.org/10.1016/0022-3697\(87\)90120-X](http://dx.doi.org/10.1016/0022-3697(87)90120-X), URL: <https://www.sciencedirect.com/science/article/pii/002236978790120X>.
- Singer-Loginova, I., Singer, H.M., 2008. The phase field technique for modeling multiphase materials. *Rep. Progr. Phys.* 71 (10), 106501. <http://dx.doi.org/10.1088/0034-4885/71/10/106501>, Publisher: IOP Publishing.
- Singh, N., Verhoosel, C.V., de Borst, R., van Brummelen, E.H., 2016. A fracture-controlled path-following technique for phase-field modeling of brittle fracture. *Finite Elem. Anal. Des.* 113, 14–29. <http://dx.doi.org/10.1016/j.finel.2015.12.005>, URL: <https://www.sciencedirect.com/science/article/pii/S0168874X15001870>.
- Suwa, Y., Saito, Y., Onodera, H., 2007. Three-dimensional phase field simulation of the effect of anisotropy in grain-boundary mobility on growth kinetics and morphology of grain structure. *Comput. Mater. Sci.* 40 (1), 40–50. <http://dx.doi.org/10.1016/j.commatsci.2006.10.025>, URL: <https://www.sciencedirect.com/science/article/pii/S0927025606003144>.
- Thieurmél, R., Besson, J., Pouillier, E., Parrot, A., Ambard, A., Gourgues-Lorenzon, A.-F., 2019. Contribution to the understanding of brittle fracture conditions of zirconium alloy fuel cladding tubes during LOCA transient. *J. Nucl. Mater.* 527, 151815. <http://dx.doi.org/10.1016/j.jnucmat.2019.151815>, URL: <https://www.sciencedirect.com/science/article/pii/S0022311519309468>.
- Verleysen, P., Peirs, J., 2017. Quasi-static and high strain rate fracture behaviour of Ti6Al4V. *Int. J. Impact Eng.* 108, 370–388. <http://dx.doi.org/10.1016/j.ijimpeng.2017.03.001>, URL: <https://www.sciencedirect.com/science/article/pii/S0734743X16310545>.
- Voigt, W., 1928. *W. Lehrbuch der kristallphysik*.

- Wang, Y., Chen, L.-Q., Khachaturyan, A., 1993b. Kinetics of strain-induced morphological transformation in cubic alloys with a miscibility gap. *Acta Metall. Mater.* 41 (1), 279–296. [http://dx.doi.org/10.1016/0956-7151\(93\)90359-Z](http://dx.doi.org/10.1016/0956-7151(93)90359-Z), URL: <http://www.sciencedirect.com/science/article/pii/095671519390359Z>.
- Wang, Y., Khachaturyan, A.G., 1995. Shape instability during precipitate growth in coherent solids. *Acta Metall. Mater.* 43 (5), 1837–1857. [http://dx.doi.org/10.1016/0956-7151\(94\)00406-8](http://dx.doi.org/10.1016/0956-7151(94)00406-8), URL: <https://www.sciencedirect.com/science/article/pii/0956715194004068>.
- Wang, S.-L., Sekerka, R., Wheeler, A., Murray, B., Coriell, S., Braun, R., McFadden, G., 1993a. Thermodynamically-consistent phase-field models for solidification. *Physica D* 69 (1), 189–200. [http://dx.doi.org/10.1016/0167-2789\(93\)90189-8](http://dx.doi.org/10.1016/0167-2789(93)90189-8), URL: <http://www.sciencedirect.com/science/article/pii/0167278993901898>.
- Wu, J.-Y., Nguyen, V.P., Nguyen, C.T., Sutula, D., Sinaie, S., Bordas, S.P.A., 2020. Chapter one - phase-field modeling of fracture. In: Bordas, S.P.A., Balint, D.S. (Eds.), *Advances in Applied Mechanics*, Vol. 53. Elsevier, pp. 1–183. <http://dx.doi.org/10.1016/bs.aams.2019.08.001>, URL: <https://www.sciencedirect.com/science/article/pii/S0065215619300134>.
- Yin, B., Steinke, C., Kaliske, M., 2020. Formulation and implementation of strain rate-dependent fracture toughness in context of the phase-field method. *Internat. J. Numer. Methods Engrg.* 121 (2), 233–255. <http://dx.doi.org/10.1002/nme.6207>, URL: <https://onlinelibrary.wiley.com/doi/abs/10.1002/nme.6207>. eprint: <https://onlinelibrary.wiley.com/doi/pdf/10.1002/nme.6207>.
- Yin, S., Yang, W., Kwon, J., Wat, A., Meyers, M.A., Ritchie, R.O., 2019. Hyperelastic phase-field fracture mechanics modeling of the toughening induced by bouligand structures in natural materials. *J. Mech. Phys. Solids* 131, 204–220. <http://dx.doi.org/10.1016/j.jmps.2019.07.001>, URL: <http://www.sciencedirect.com/science/article/pii/S0022509619300584>.
- Zhang, Y., Lorentz, E., Besson, J., 2018. Ductile damage modelling with locking-free regularised GTN model. *Internat. J. Numer. Methods Engrg.* 113 (13), 1871–1903. <http://dx.doi.org/10.1002/nme.5722>, arXiv:<https://onlinelibrary.wiley.com/doi/pdf/10.1002/nme.5722>.
- Zhao, Y., Ai, S., Fang, D., 2018. Elasto-plastic phase field modelling of oxidation of zirconium alloys. *Int. J. Solids Struct.* 134, 30–42. <http://dx.doi.org/10.1016/j.ijsolstr.2017.10.033>, URL: <http://www.sciencedirect.com/science/article/pii/S0020768317304924>.
- Zhou, F., Molinari, J.F., 2004. Dynamic crack propagation with cohesive elements: a methodology to address mesh dependency. *Internat. J. Numer. Methods Engrg.* 59 (1), 1–24. <http://dx.doi.org/10.1002/nme.857>, URL: <https://onlinelibrary.wiley.com/doi/abs/10.1002/nme.857>. eprint: <https://onlinelibrary.wiley.com/doi/pdf/10.1002/nme.857>.